https://doi.org/10.5194/egusphere-2026-4872
Preprint. Discussion started: 19 August 2026

The NASA Aerosol Wind Profiler Doppler Wind Lidar, Part I: Instrument Description and Airborne Demonstration

Kristopher Bedka[1], John Marketon[1], Sammy Henderson[2], Konstantin Khlopenkov[3], John Cooney[1], Michael Kavaya[1], Samantha Applin[1], F. Guy Wilson[1], Seth Begay[1], Maurice Cross[1], Joe Diamond[2], Anjie Emmett[1], G. David Emmitt[4], Steven Greco[4], Patrick Kratovil[3], Anna Noe[1], and Aboubakar Traore[1]

[1] *NASA Langley Research Center, Hampton, Virginia 23666 USA*

[2] *Beyond Photonics LLC, Boulder, Colorado 80301 USA*

[3] *Analytical Mechanics Associates, Hampton, Virginia 23666 USA*

[4] *Simpson Weather Associates, Charlottesville, Virginia 22902*

Correspondence to: Kristopher Bedka (kristopher.m.bedka@nasa.gov)

Abstract

There is a well-recognized need for new orbital 3-dimensional (3-D) wind measurements to improve weather prediction and understanding of atmospheric processes. A new airborne, coherent-detection Doppler wind lidar system called the Aerosol Wind Profiler (AWP) has recently been developed at NASA to address community wind measurement needs and demonstrate technologies needed for an orbital wind lidar mission, leveraging decades of NASA Langley Research Center and industry partner experience with wind lidar instrumentation. This paper describes the AWP instrument, data collection methods, and 3-D wind profile retrieval methods applied to data from its first science campaigns that occurred from September-November 2024. Additional demonstrations of AWP observations and their validation are provided in Part II of this paper.

1. Introduction

1.1. Community Needs for 3-D Wind Profile Measurements

Measurements of 3-D winds, defined here as vertical profiles of horizontal wind fields, are necessary for understanding and improving prediction of sensible and latent heat fluxes, aerosol, dust, smoke, and pollution transport, cloud formation/evolution, cyclones, severe thunderstorms, and many others. Conventional wind profiles from commercial aircraft, weather radars, microwave profilers, and radiosondes are sparse in space and time (Baker et al. 2014). New profiling methods are especially needed for the planetary boundary layer (PBL), the turbulent layer adjacent to the Earth's surface where wind, temperature, and moisture observations are currently lacking or inadequate (Teixeira et al. 2025). Improving wind profiling is especially critical for diagnosing and predicting extreme weather events that adversely impact society. For example, it has been found that wind profile information within and above the PBL is necessary for discriminating tornadic vs. non-tornadic supercell thunderstorms (Coniglio and Parker 2020), diagnosing hailstorm environments (Nixon and Allen 2022; Taszarek et al. 2026), understanding vertical wind shear impact on tropical cyclone intensification (Rios-Berrios et al. 2024), and predicting flooding rainfall events from atmospheric rivers (Pagano et al. 2021).

Wind estimates derived from satellite imager atmospheric motion vectors (AMVs) and feature tracking of satellite infrared/microwave sounder profiles (Santek et al. 2019; Zeng et al. 2024) augment conventional wind observations

https://doi.org/10.5194/egusphere-2026-4872
Preprint. Discussion started: 19 August 2026

(Stoffelen et al. 2020). Imager AMVs have had significant positive impact on numerical weather prediction (NWP) model performance for many years (Eyre et al. 2022). AMVs originate from cloud or water vapor tracer motions, providing limited vertical profile information only when clouds of varying height are in proximity, or when a trackable mid- to upper-tropospheric water vapor tracer overlays lower clouds. Sounder wind profile retrievals are envisioned to provide greater vertical coverage, especially when advanced feature tracking methods like optical flow are employed (Yanovsky et al. 2024). Initial experience with deriving 3-D wind fields with sequential NOAA-20 and Suomi-NPP infrared and microwave sounder water vapor profiles on one day using an optical flow algorithm revealed that ~7700 profiles from 100 hPa to the surface featured entirely successful wind retrievals, a factor of ~6 greater than the number of global radiosonde profiles per day. The root-mean-squared difference (RMSD) between the sounder 3-D vector wind retrieval and co-located radiosonde measurements was 7.7 m/s (Ouyed et al. 2025). Future infrared (microwave) sounder technology is expected to offer 1.5-2.0 km (2.0-3.0 km) vertical resolution (Zeng et al. 2024). Future sounder wind and radiance observations are certain to have significant impact on NWP and our understanding of atmospheric processes (McCarty et al. 2021), and wind profile precision is expected to improve when sounder profiles are more closely spaced in time than those studied by Ouyed et al. (2025) (Yanovsky et al. 2024). But their vertical resolution and measurement precision may not be able to sufficiently depict PBL dynamics especially when the PBL is shallow or in weak wind conditions, so additional wind measurement approaches are needed.

The 2017 Decadal Survey (National Academies of Sciences, Engineering, and Medicine, 2018) concurred that existing space-based wind measurements are insufficient and recommended new orbital 3-D wind profilers in the 2017-2027 Survey timeframe. Wind profile measurements were necessary to address 19 Earth Science and Earth Application Objectives in the Decadal Survey (Table B.1 Consolidated Science and Applications Traceability Matrix), while many more of these objectives require near-surface wind measurements. The need for 3-D winds is also documented in the NOAA Satellite Observing System Architecture study (NSOSA, NOAA NESDIS 2018). The NSOSA study referred to 3-D wind profile measurements as being the "Holy Grail of NWP". NOAA seeks 3-D wind data every 3-24 hours at 15-400 km horizontal and 0.5-4 km vertical resolution, with 2-10 m/s precision (Table 2 of NOAA NESDIS 2022). Similar measurement requirements are specified by the World Meteorological Organization for global numerical weather prediction and real-time weather monitoring (WMO OSCAR, 2025).

1.2. A Role for Doppler Wind Lidar within the Global Wind Observing System

Doppler wind lidars (DWLs) have the unique ability to measure wind profiles with high vertical resolution and precision in both cloudy and clear sky conditions. A DWL has also been referred to as the "missing link in the Global Observing System" (Baker et al. 2014). There has been an extensive array of Observing System Simulation Experiments (OSSEs) and Observing System Experiments (OSEs) that investigated the potential impact of DWLs on numerical weather prediction (NWP) model performance. The experiments had been done to support orbital mission concepts such as the Global Wind Observing System (GWOS, Riishojgaard et al. 2012; Ma et al. 02015), Optical Autocovariance Wind Lidar (OAWL, Atlas et al. 2015), NASA Langley Research Center and Japanese coherent-detection wind lidar concepts (Ishii et al. 2017, Baron et al. 2017; Okamoto et al. 2018; Karpowicz and Prive 2024), and the European Space Agency (ESA) Aeolus mission (Marseille et al. 2007, 2008). These studies agreed that DWLs

https://doi.org/10.5194/egusphere-2026-4872
Preprint. Discussion started: 19 August 2026

would significantly improve NWP model performance. A greater number of satellites carrying DWLs at varying overpass times, or a single DWL with multiple viewing perspectives (or "lines-of-sight" (LOS)) were found to have greater impact than just a single satellite with a single LOS (Marseille et al. 2008; Ma et al. 2015). Karpowicz and Prive (2024) found that DWL impact from a NASA space mission concept greatly depends on assumed lidar backscatter sensitivity, spatial scale of breaks in cloud cover, and the lidar ability to penetrate through non-opaque cloud.

Positive DWL impact on NWP was demonstrated with Aeolus, the first-ever orbital DWL mission (ESA 2023). Rennie et al. (2021) found that assimilation of Aeolus LOS wind speed profiles provided statistically significant improvement in short-range forecasts by the European Centre for Medium-range Weather Forecasts (ECMWF) global model. Longer forecast range verification showed positive impact strongest at the day two to three forecast range, most notably in the tropical upper troposphere and lower stratosphere, and polar troposphere. Lower than expected Aeolus atmospheric signal detection led to solar background noise dominating Rayleigh wind error (Rennie et al. 2021; Lux et al. 2025) and reducing Mie channel sensitivity to only detect clouds and very optically thick aerosol plumes (Flament et al. 2021). Mie winds provided comparable or greater impact compared to Rayleigh later in the Aeolus mission due to better precision (3-4 m/s Mie vs 5-7 m/s Rayleigh, Rennie 2023). Aeolus-2, with a launch in the 2030s, is expected to provide higher resolution and precision to generate an even greater NWP impact (Heliere et al. 2023).

Given the DWL impact, development of DWL technologies and instruments for ground, airborne, and space operation has been ongoing for several decades. DWLs have employed two sensing methods: direct-detection and coherent- (or "heterodyne-") detection. Direct detection DWLs typically operate in the 355 to 1064 nm range, and measure the intensity of backscatter signal, employing an interferometer for Doppler shift discrimination. The Aeolus mission carried the ALADIN direct-detection DWL operating at a 355 nm UV wavelength and demonstrated that space-based DWL profiling is possible (Straume-Lindner et al. 2021). Coherent-detection DWLs (CDWLs) have typically operated in the 1.5 to ~10 µm range, and have been widely used from the ground and aircraft for a variety of applications (Rew et al. 2025). CDWLs operate by mixing (or "heterodyning") atmospheric backscatter signal with a local oscillator. The resulting intermediate frequency "beat" signal is processed using a Fast Fourier Transform (FFT) from which aerosol backscatter intensity and the Doppler shift required for wind measurement are derived.

Lidar theory and community experience with DWLs demonstrate that CDWLs can be used to attain especially high spatial/vertical resolution and precision wind profiles (Henderson et al. 2005; Lux et al. 2022). Experience with a 2 µm CDWL at the German Aerospace Center DLR led to the conclusion that a CDWL is suitable to assess the quality of other wind observations due to the low measurement error originating from heterodyne detection (Witschas et al. 2022). A comparison of coherent and direct detection receivers is described by Henderson et al. (2005). In short, key advantages of CDWL receivers include immunity from background solar radiation and detector noise (dark current), and high-efficiency, high-spectral-resolution detection of narrowband heterodyne signals from Mie scattering in the radio frequency domain, allowing high-sensitivity signal detection and frequency measurement in the digital domain. Mie signal from aerosol or cloud backscatter has significantly narrower Doppler velocity spread than Rayleigh scattering from atmospheric molecules, a result of significantly less Brownian motion in the atmosphere due

https://doi.org/10.5194/egusphere-2026-4872
Preprint. Discussion started: 19 August 2026

to the larger size and mass of aerosol particles compared to molecules. The velocity (frequency) spread of Mie backscattered light is limited by wind velocity variation in the measurement volume and by the spectral width of the transmitter pulse rather than by Brownian motion. Doppler spreads are typically on the order of 1 m/s for aerosol particles and 300 m/s for atmospheric molecules. Due to the narrow bandwidth of the signal, if the Mie signal return above instrument noise level is detected by a CDWL, it will measure winds with high precision (≤ 1 m/s, assuming that the pulse duration is sufficiently long) *even with a single lidar pulse*, providing the potential for extremely high-resolution wind measurements (Frehlich et al. 1994). Signal averaging ("integration") across many CDWL pulses is used to reduce instrument noise in the wind retrieval process, improving sensitivity to weak backscatter conditions (Frehlich et al. 1997; Frehlich 2004) and further improving the velocity measurement precision. In both coherent- and direct-detection, the signal return intensity modulates the backscatter sensitivity and vertical coverage of successful wind profiles.

1.3. NASA Langley CDWL Technology Development

NASA Langley Research Center (LaRC) and partners have been developing CDWL technology for over two decades (Yu 2006; Singh et al. 2015). LaRC's first CDWL instrument, the Doppler Aerosol WiNd lidar (DAWN, Kavaya et al. 2014), flew in eight NASA airborne science campaigns from 2010-2022. DAWN was used for Arctic region PBL wind measurements (Duvivier et al. 2017; Greco et al. 2020a), tropical cyclone and convection research (Kavaya et al. 2014; Turk et al. 2020; Greco et al. 2020b; Hristova-Veleva et al. 2021; Sakaeda et al. 2024, 2025; Feng et al. 2025; Mazza and Chen 2025; Lee et al. 2026), Saharan dust transport measurements (Nowottnick et al. 2024), and underflights and validation of the space-borne ESA Aeolus wind lidar (Bedka et al. 2021). DAWN showed precision as high as 1.2 m/s relative to dropsonde during the 2019 NASA Aeolus Cal/Val Test Flight campaign (Bedka et al. 2021). DAWN operated on NASA's DC-8 and UC-12B aircraft, but both are now retired. DAWN was too large and heavy to fly on smaller aircraft such as NASA's Gulfstream-III which necessitated development of a new airborne DWL.

Building on experiences with DAWN and DWL technology, LaRC, Beyond Photonics LLC, Simpson Weather Associates, and Fibertek Inc. were funded by the NASA Earth Science Technology Office (ESTO) to develop a next-generation DWL transceiver called the Wind-Space Pathfinder (Wind-SP). The primary foci of the Wind-SP program were to assess the feasibility of a CDWL aboard the International Space Station, develop and demonstrate key CDWL subsystems and technologies that have the highest risk for space, and demonstrate a CDWL incorporating advanced subsystem technologies. The Wind-SP project extended from April 2017-2022 with a substantial delay from COVID-19. The Wind-SP concept involves transmitting laser pulses into two telescopes with LOS's oriented 90° apart in the fore- and aft-direction (45° and 135° azimuth) relative to a spacecraft orbit. Lidar pulses with ~60 mJ energy alternate between the two LOS at 200 Hz, enabling vertical profiling of aerosol/cloud backscatter intensity and wind vectors derived from the two LOS wind speed profiles. Many technologies needed for an orbital CDWL were developed, including: improved transmitters with high pulse energy and pulse repetition rate for long range wind measurements (Yu et al. 2022; Henderson et al. 2022); auto-alignment sensors and actuators for maintenance of optimal CDWL performance and orbital lag-angle compensation; electronic, non-mechanical beam path selection enabling two LOS

https://doi.org/10.5194/egusphere-2026-4872
Preprint. Discussion started: 19 August 2026

for wind vector measurements; and compact highly-stable and tunable reference lasers allowing for high-precision velocity measurement at long ranges (e.g. ≥ 400 km) while mitigating the impact of platform velocity (Henderson et al. 2022). The Wind-SP project completed a fully functioning CDWL transceiver with a figure of merit ~3-4x greater than DAWN (Figure 1 and Section 2.1, Table 2). It was found that an orbital Wind-SP transceiver would have sufficient aerosol backscatter sensitivity to enable high vertical (0.1-1 km) and horizontal (10-100 km) resolution aerosol and wind profiling (Bedka et al. 2025, see Section 5.2 of this paper for more detail).

1.4. The NASA Aerosol Wind Profiler (AWP) and Airborne Observations

During the Wind-SP program, a project began to integrate Wind-SP into a next-generation airborne CDWL called the Aerosol Wind Profiler (AWP, Bedka et al. 2024). AWP configures the two beam paths of Wind-SP for off-nadir vertical profiling of horizontal wind vectors and nadir profiling of vertical motions. The AWP instrument is comprised of a lidar transceiver, an enclosed structure containing beam routing optics and two parallel telescopes, and a rotating beam-steering assembly for the off-nadir beam (Figure 1). Custom-designed aircraft interface adapters mount AWP to various research aircraft.

AWP was first flown on engineering test flights aboard the NASA LaRC Gulfstream-III (G-3) in January 2023 and the DC-8 in October 2023 (Bedka et al. 2024). AWP was then flown aboard the G-3 from 20 September to 16 October 2024 under the NOAA "Measuring the Atmospheric Wind profile (3-D Winds): Call for Studies and Field Measurement Campaigns for NOAA/NESDIS" Broad Agency Announcement (NOAA NESDIS 2022) 3-D Wind Demonstration Mission to demonstrate how a CDWL could meet NOAA wind observation requirements. It was also flown from 27 October – 15 November 2024 during the NASA Westcoast & Heartland Hyperspectral Microwave Sensor Intensive Experiment (WH^{2}yMSIE) – Active Passive PBL profiling Experiment (APEX) (Bedka et al. 2025). The NASA LaRC High Altitude Lidar Observatory (HALO) flew with AWP during these campaigns, configured with a four-wavelength differential absorption lidar (DIAL) transmitting near 935 nm for water vapor profiling (Caroll et al. 2022), and a 1064 nm backscatter and 532 nm high-spectral-resolution lidar (HSRL, Hair et al. 2008) for aerosol/cloud profiling. The Fall 2024 AWP flight datasets will be briefly introduced later in this Part I paper, and more comprehensively described in Part II of the paper (Bedka et al. 2026).

This paper focuses on a description of the AWP instrument, 3-D aerosol cloud backscatter intensity and wind retrieval methods, and selected wind profile datasets from Fall 2024 G-3 flights. Section 2 describes the AWP instrument, Section 3 describes data collection and wind retrieval methods. Section 4 highlights data collected during a NOAA Joint Venture 3-D Wind Demonstration flight. Section 5 summarizes the paper and describes future development activities.

https://doi.org/10.5194/egusphere-2026-4872
Preprint. Discussion started: 19 August 2026

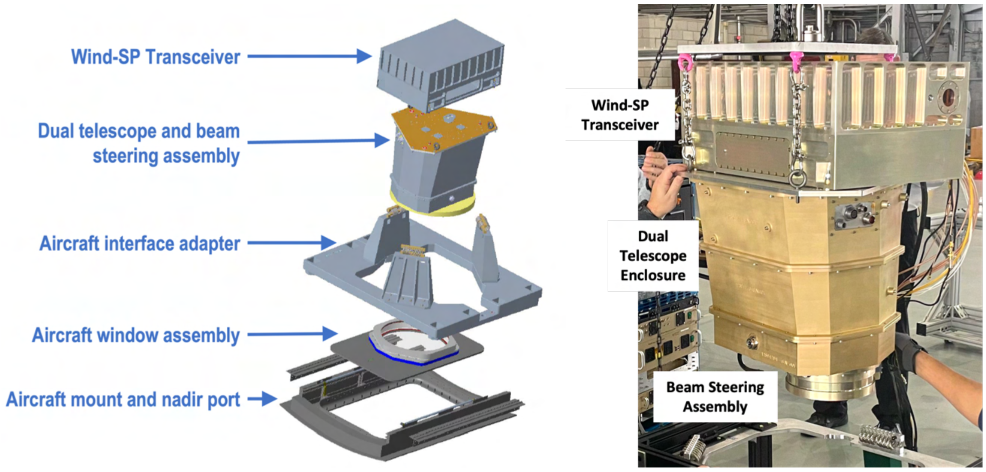

Figure 1: (left) A schematic of the AWP instrument and components required for aircraft integration. (right) A photo of AWP hoisted above its instrument transport cart.

2. AWP Instrument Description

The AWP / Wind-SP (AWP hereafter) CDWL is a monostatic lidar with shared transmit/receive optics (Wang, 1988; Henderson, 2005) comprised of four key components: a High-Power Module (HPM), a pump laser, a Low Power Module (LPM), and electronics subsystems. The electronics are dispersed throughout the HPM, LPM, and other external enclosures. These modules are described in detail in the sections below. Figure 2 provides a schematic diagram of the AWP. The HPM, which is the Wind-SP transceiver, is housed in a sealed ~64 x 41 x 27 cm enclosure, located atop the AWP (Figure 1). The HPM contains the pulsed high-power transmitter optics, receiver optics, and a Local Electronics Module (LEM). The HPM produces two 6 mm diameter lidar beams, which are routed to a pair of telescopes that expand the beams to a 120 mm diameter in the 150 mm aperture of each telescope. One beam is configured to exit the lidar and aircraft vertically for measurements of w-component vertical wind profiles, while the second beam is configured to pass through a beam steering prism that deflects 30° off nadir for profiling of u- and v-component horizontal wind vectors. AWP is mounted at an angle to compensate for the typical aircraft angle of attack (2.5° for the NASA G-3), such that the nadir beam is as close as possible to perpendicular with the Earth surface. The overall instrument has dimensions of 80 x 60 x 40 cm (Figure 1-right). The orbital instrument configuration directs the two beams into two telescopes oriented 30° off-nadir and 90° apart in azimuth for horizontal wind vector profiling without the need for beam steering. The LPM is housed in a 2U enclosure mounted in an equipment rack which contains the continuous wave (CW) reference lasers and control electronics, offset locking circuits, and the lidar optical fiber network. Key AWP lidar specifications and attributes are provided in Table 1.

https://doi.org/10.5194/egusphere-2026-4872
Preprint. Discussion started: 19 August 2026

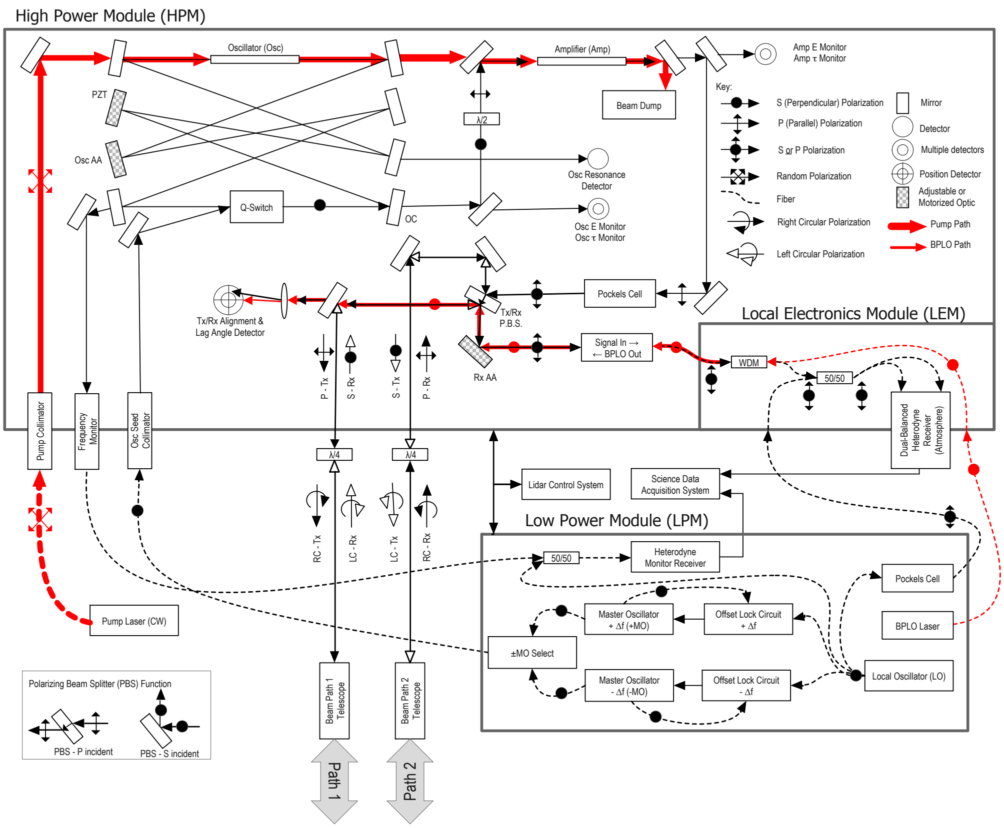

Figure 2: A schematic diagram of the AWP lidar system.

Category	Specification
Laser Crystal	Ho:LuLF
Wavelength	2052.92 nm
Pump Geometry	End-pumped Master Oscillator – Power Amplifier (MOPA)
Pump Source	Thulium fiber laser, 1938 nm
Pump Power	53 W required to achieve 40 mJ
Pulse Energy	~40 mJ during 2024 Flights, Capable of 60 mJ
Pulse Rate	200 Hz
Average Optical Power	8 W @ 40 mJ/pulse
Pulse Duration FWHM	250 ns @ 40 mJ/pulse, decreases with increasing pulse energy
Signal Optical Detector	Extended InGaAs, room temperature
Beam Quality M^2	1.07
Laser Oscillator Cavity	3.6 m folded cavity
AWP Dimensions	80 x 60 x 40 cm
Instrument Mass	110 kg
Telescope Design	f/8, four mirror folded, off-axis Cassegrain design, ø15 cm primary aperture, 20x expansion ratio
Telescope Dimensions	34 x 36 x 19 cm
Digitization Rate	500 Mega-samples/second

Table 1: A summary of attributes and specifications of the AWP Doppler wind lidar system.

https://doi.org/10.5194/egusphere-2026-4872
Preprint. Discussion started: 19 August 2026

2.1. High-Power Module (HPM)

Wind velocity measurement accuracy and backscatter sensitivity drive key transmit laser pulse characteristics, namely beam quality, and pulse duration, energy, and repetition frequency. The AWP pulsed transmit laser has an injection-seeded, Q-switched Ho:LuLF, Master Oscillator Power Amplifier (MOPA) architecture (Yu et al. 2022). The current configuration generates pulses with ~40 mJ energy, 250 ns duration, and a beam quality of ≤1.07 M^2. A schematic of the HPM is provided in Figure 2 (top section). All optical components are arranged on a carbon fiber composite (CFC) optical bench, with the pump laser coupler and beam shaping optics mounted on the bottom and all remaining components mounted on the top. Both oscillator and amplifier crystals are end-pumped by a Thulium fiber pump laser operating at 1938 nm (Section 2.4, Yu et al. 2022; Henderson et al. 2022). The oscillator crystal absorbs about half of the pump energy, with the remainder passing through to the amplifier. The crystals are liquid-cooled to 17°C by an external chiller unit. The required pulse length is the key driver for the 3.6 m oscillator cavity length, which is folded into an 8-mirror bowtie geometry. A +27-MHz intra-cavity Acousto-Optic Modulator (AOM) is used to Q-switch to modulate the laser. To establish single-mode lasing at the desired wavelength, the oscillator laser is seeded by a CW master oscillator (MO, Section 2.4) reference laser that is injected into the cavity through the Bragg diffraction axis of the AOM. A modified version of the ramp and fire injection seeding servo (Henderson et al., 1986) is used to ensure the oscillator is successfully seeded so it produces single frequency pulses. The injection-seeded oscillator generates ~20 mJ pulse energy, with the amplifier doubling the output energy without significantly degrading beam quality. The transmit laser is stable in both time and frequency. Jitter is estimated to be less than ~50 ns in time and less than 1 MHz in frequency. Oscillator pulse energy and the pulse temporal profile are monitored by the lidar control system. A motorized tip-tilt mount with position feedback enables some remote adjustment capability that can be used to optimize the laser cavity. This mount is a key component of the Auto-Alignment system (Section 2.5).

Pump light not absorbed by the oscillator crystal is used to pump the amplifier crystal. To maximize absorption of the residual pump light in the amplifier crystal its crystal axes are rotated by 90° with respect to the oscillator crystal. Specifically, in the oscillator, the Ho:LuLF crystal axis is along the S-polarization whereas in the amplifier it is along the P-polarization axis. Due to the amplifier crystal rotation, the S-polarized laser pulse exiting the oscillator is rotated to P-polarization using a λ/2 plate, allowing the amplifier gain to be maximized. Dichroic mirrors, highly reflective (HR) for 2.053 µm light, but transparent (T) to 1.938 µm light, allow the pump light to be routed into the oscillator and amplifier crystals while routing the transmit laser pulse appropriately. The amplifier absorbs about half of the total pump power, and any remaining pump light is routed into a beam dump via an HR 1.938 µm / T 2.053 µm dichroic mirror. Amplifier pulse energy and temporal profile are monitored by the lidar control system.

On exiting the amplifier, the transmit laser pulse is routed to a Pockels Cell, which sets the pulse to S- or P-polarization as specified by the lidar control system. The transmit/receive switch is a polarizing beam splitter (Tx/Rx PBS) reflecting incident S-polarized light while transmitting P-polarized light. P-polarized light is routed to lidar beam path 1, passing through a λ/4 plate for conversion into right circular (RC) polarization, then to a beam expanding telescope for 20x expansion and transmission into the atmosphere (Section 2.6). The fraction of the atmospheric return signals that are not depolarized by the scatterers arrive with left circular (LC) polarization at the telescope and are

https://doi.org/10.5194/egusphere-2026-4872
Preprint. Discussion started: 19 August 2026

compressed by the same 20x factor. The λ/4 plate converts the returning atmospheric light to S-polarization, which the Tx/Rx PBS reflects into the receiver. Functionally, beam path 2 is configured similarly, with S-polarized light converted to LC for transmission into the atmosphere, and the RC return light converted to P-polarized light. The Tx/Rx PBS transmits the P-polarized return light into the receiver. One mirror in beam path 1 is a 1.55 µm T / 2.053 µm HR dichroic, which allows leakage of a small amount of P-polarized light to be used for Tx / Rx beam path alignment (Section 2.5). A mirror mounted to a motorized tip-tilt mount with position feedback is located between the Tx/Rx PBS and the receiver. This enables remote adjustment of the receive beam path to the P-polarized transmit beam path, another key component of the Auto-Alignment system.

AWP pulse energy is modulated by the pump laser power input into the pulsed laser cavity and amplifier. The laser demonstrated 75 mJ/pulse during laboratory development on an optical table. During development, the CFC optical bench was found to outgas polyacrylonitrile (PAN), a carbon-fiber precursor material, which contaminated laser optical surfaces. Laser induced damage occurred on mirror surfaces with high fluence when operating at ~60 mJ/pulse (12 W, orbital instrument baseline energy specified by the Wind-SP program). It was experimentally determined that damage did not occur when operating at ≤ 40 mJ/pulse (8 W, orbital instrument threshold energy), an energy generated throughout the Fall 2024 flights from 55 W of pump light. A second AWP transceiver is currently being built on an Invar bench, which being metallic does not outgas, permitting ~60 mJ/pulse but with slightly shorter pulse duration (~200 ns) that occurs in conjunction with higher pulse energy. We note that CFC benches have been successfully used in other coherent lidar transceivers (see Figure 7.42 in Henderson et al., 2005) with laser fluence on some internal optics higher than any fluence levels in the AWP transceiver, even at 60 mJ pulse energy. Thus, a significantly-lower-mass bench option for the future is CFC, but with additional process control during manufacturing to eliminate contamination potential. We decided to implement the Invar bench in the second AWP transceiver in the near term since it was a faster, lower-cost, and lower-risk alternative to a new CFC bench design, build process, and associated testing to ensure sufficiently low levels of contamination.

A metric used to compare CDWL performance of laser transmitters with varying specifications such as pulse energy, repetition frequency, duration, and beam quality is the transmitter figure of merit (TFOM), which is inversely proportional to the minimum CDWL backscatter sensitivity. The TFOM metrics for DAWN and AWP cited in Table 2 is given by:

$$TFOM = \frac{2}{1+(M^2)^2} \cdot E \cdot \sqrt{PRF} \cdot \tau^{0.5-\alpha}$$

where E is the pulse energy, PRF is the pulse repetition frequency, τ is the pulse FWHM duration, and M^2 is the beam quality factor (times diffraction limited far field beam divergence). This representation of the TFOM, which includes the impact of the pulse duration and an additional factor of 2 in the first factor, is a modification of the FOM from Dolfi-Bouteyre et al. (2009). For typical CDWL pulse durations, the mean signal peak height in the spectrum is proportional to $\frac{2}{1+{M^2}^2} \cdot E \cdot \tau$. Including 2 in the numerator of the TFOM expression is optional, but we choose to include it since the first term then more directly describes the efficiency factor of the lidar as a function of the beam quality factor, M^2. The $\sqrt{PRF}$ dependence of TFOM is due to a reduction in noise fluctuations from averaging over multiple pulses within the required measurement time. In many realistic measurement scenarios aimed at making

https://doi.org/10.5194/egusphere-2026-4872
Preprint. Discussion started: 19 August 2026

useful measurements in weak signal conditions (i.e. at longer ranges or lower backscatter levels), multiple range gates are also averaged to further reduce the noise fluctuations. Since the intrinsic range resolution of the lidar is proportional to the pulse duration, the number of independent intrinsic range resolution gates that can be incoherently averaged within a fixed range resolution requirement for the measurement is inversely proportional to τ. Therefore, range gate averaging results in another $\sqrt{1/\tau}$ factor in the TFOM due to the additional reduction in noise fluctuations. The additional $\tau^{-\alpha}$ factor in the TFOM arises from detecting signals with varying spectral width in white noise over a fixed frequency search band. The SNR required to successfully detect the signal peak in the noise increases as the ratio of the frequency search bandwidth to the signal spectral bandwidth increases. Analysis and numerical modeling indicates that, for probability of a good signal peak detection (P_g, see Section 3) of 50%, $\alpha \approx 0.22$ and for P_g=90%, $\alpha \approx 0.13$. As P_g approaches 100%, α approaches zero. It is important to note that the $\tau^{0.5-\alpha}$ factor in the TFOM assumes that the transmitter produces near-transform-limited laser pulses (i.e. with spectral width scaling inversely with the pulse duration) and that the spectral width of the lidar signal is dominated by the spectral width of the transmit pulses. This is usually the case for shorter laser pulses that are typically used in well-designed CDWL systems. For longer pulses the spectral width of the signal eventually is dominated by wind turbulence in the measurement volume and the $\tau^{0.5-\alpha}$ dependence is no longer valid. In many, but not all, measurement scenarios, the TFOM defined above is a good indicator of performance for pulse durations less than ~500 ns. When the signal spectral width is dominated by other factors there is no lidar performance benefit in using longer pulse durations. The lidar specifications and TFOM for DAWN as operated during the 2022 CPEX-CV campaign (Nowottnick et al. 2025), AWP CFC, and AWP Invar are listed in Table 2. TFOM values listed in Table 2 are for $P_g = 90\%$. The TFOM indicates that AWP CFC provides 2.9x better performance than DAWN. AWP Invar is expected to be 4x better than DAWN.

Parameter	DAWN	AWP CFC	AWP Invar
Pulse Energy (E, mJ)	80	40	60
Pulse Repetition Frequency (PRF, s^{-1})	10	200	200
Pulse Duration (τ, ns)	180	250	200
Beam Quality (M^2)	1.1	1.07	1.07
Transmitter Figure of Merit (TFOM)	1.56	4.55	6.28
Normalized TFOM Relative To DAWN	1.0	2.91	4.02

Table 2: Operating parameters for DAWN, AWP CFC Bench, and expected performance from the AWP Invar Bench.

2.2. Thulium Fiber Pump Laser

The energy source for the AWP pulsed laser is an external CW Thulium-fiber laser operating at 1938 nm. The pump laser output is routed to the AWP HPM through an optical fiber. For development and laboratory work, as well as for airborne operations, the pump laser used is a commercially available, randomly polarized, 100 W Tm-fiber laser

https://doi.org/10.5194/egusphere-2026-4872
Preprint. Discussion started: 19 August 2026

from IPG Photonics (Figure 3, right). A TRL-5, space-qualifiable, conductively cooled pump laser was delivered by Fibertek for Wind-SP (Figure 3, left), which generates 100 W of linearly polarized, 1938.6 nm laser light. This pump laser offers electrical to optical efficiency > 22%, with a beam quality of $M^2 < 1.1$. Linearly polarized light results in improved (compared to the IPG) pumping of the Ho:LuLF gain medium. This pump laser is 27.5 x 35 x 11.25 cm and has a mass of 13.6 kg. Further description is provided by Engin et al. (2020).

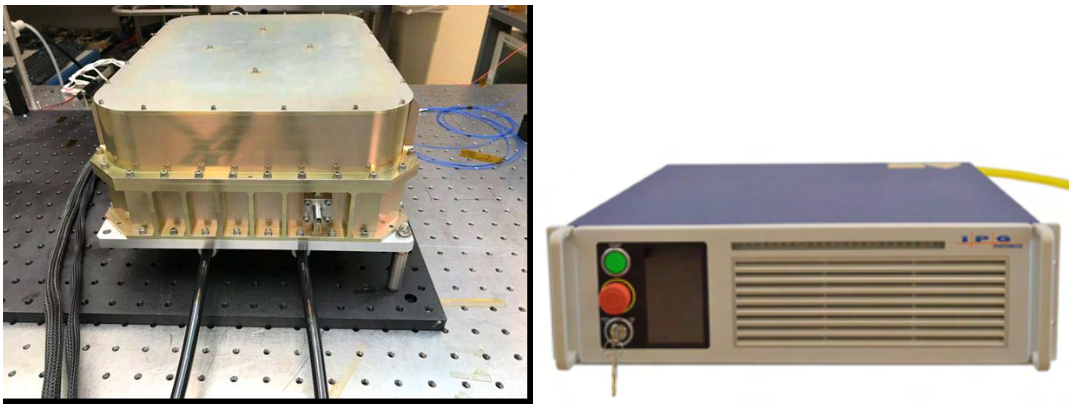

Figure 3: ***(left) Fibertek space-qualifiable Tm fiber pump laser intended for space-based operation (Engin et al. 2020). (right) IPG Photonics 100 W Tm fiber pump laser implemented with AWP.***

2.3. Local Electronics Module (LEM) and Heterodyne Receiver

The LEM contains high-voltage drivers, transceiver health and monitoring electronics, and several key receiver system components. The high-voltage driver powers the Pockels cell controlling transmit pulse polarization, and installation in the LEM minimizes high-voltage wiring (Figure 4). Transceiver health and monitoring includes pressure, temperature, humidity, and oscillator and amplifier pulse energies. An acquisition and processing board is embedded in the LEM to capture these parameters and subsequently transmit them to the lidar control electronics via RS-422 communication. Also contained in the LEM is the atmospheric dual-balanced heterodyne receiver and its 50/50 coupler, plus a wavelength division multiplexer (WDM) that is part of the Auto-Alignment system (Section 2.5).

A key CDWL component is a dual-balanced heterodyne receiver. The Doppler shift from aerosol backscatter signals is on the order 2 picometers from typical airborne platforms (and as much as 50 pm from envisioned space platforms), and needs to be measured to an accuracy on the order of 10 femtometers. The return signal strength that is detected with only a few pulses averaged is on the order of a 1 picowatt (10 photons/µs) and the minimum sensitivity of the lidar is 1-10 femtowatts (0.01 - 0.1 photons/µs); the specific level depending on the amount of averaging over pulses and range gates that is utilized. Direct detection of these extremely small wavelength changes in extremely weak return signals is possible but challenging and inevitably leads to complex optical systems, signal detectors, and electronics. Heterodyne detection is a well-established technique to measure small and weak Doppler shift signals by mixing a reference signal with the return signal to generate an easily detectable intermediate frequency (IF). Details on the heterodyne detection process are provided by DeLange (1968) and Rew et al. (2025).

https://doi.org/10.5194/egusphere-2026-4872
Preprint. Discussion started: 19 August 2026

There are two key elements to the AWP heterodyne receiver: a 50/50 fiber optic coupler/splitter ("fiber coupler" hereafter) and the dual-balanced receiver. The atmospheric return signal arrives at the receiver fiber coupler telescope aperture and is condensed and injected into the receiver single-mode fiber. The return signal passes through the WDM and is injected as one input to the 50/50 coupler. The local oscillator (LO) signal, generated in the LPM (Section 2.4), is injected as the second input to the 50/50 coupler, which optically mixes and amplifies the atmospheric signal with the LO. The resulting signal is evenly split between the two output fibers, which are connected to the inputs of the dual-balanced receiver. Room-temperature extended-range InGaAs detectors heterodyne the mixed signal, generating an IF that corresponds to the beat frequency between the LO and the atmospheric signal. With sufficient LO power, LO shot noise dominates all other noise sources, such as detector dark current, detector background light, and amplifier noise. The dual-balanced receiver architecture inherently cancels excess LO intensity noise (other than shot noise), allowing for near quantum shot-noise limited detection. The 50/50 signal/LO coupler minimizes the LO power requirement.

The AWP 2.053 μm laser wavelength corresponds to a carrier frequency of ~146 THz; optical heterodyning down-converts these THz input signals to a ~100 MHz IF range. After additional amplification and bandpass filtering over the 25 – 245 MHz IF range, the balanced receiver output is sent to the Science Data Acquisition System, which digitizes signals at 500 mega-samples per second (MS/s). The offset frequency is set such that zero wind speed occurs at the mid-point of the receiver passband, or ~ 135 MHz. A 0.974 MHz Doppler shift corresponds to ~1 m/s wind speed, resulting in a detectable LOS wind speed range of ± 112.9 m/s. In practice, the bandwidth combined with the 30° off-nadir deflection of the beam used for horizontal wind profiling would enable a +/- 130 m/s measurement range, assuming negligible a vertical wind component.

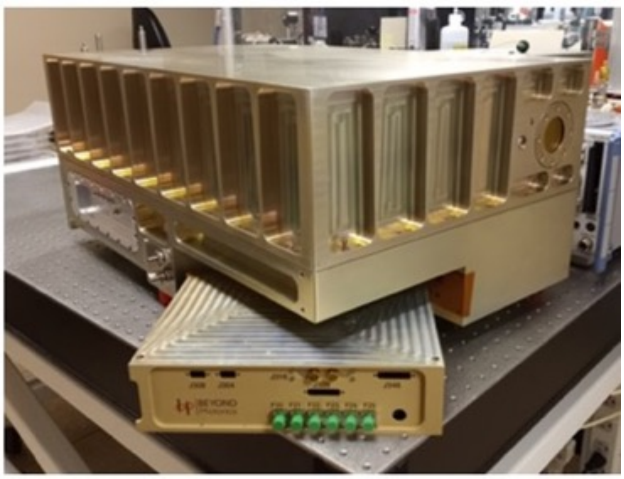

Figure 4: The AWP Local Electronics Module partially removed from the HPM.

2.4. Low-Power Module (LPM)

The LPM contains three Swift (Super-WIde Frequency-Tunable) CW solid-state lasers developed by Beyond

https://doi.org/10.5194/egusphere-2026-4872
Preprint. Discussion started: 19 August 2026

Photonics that serve as reference lasers (Henderson and Hale 2017). The LPM also contains the Swift electronics, two offset lock circuits, the BPLO (Section 2.5), a control card, heterodyne monitor detector, and the lidar fiber optic network. All components are attached to a thermal plate connected to the AWP chiller.

One Swift is configured as the LO, generating the primary lidar reference signal at 2052.92 nm within one of several atmospheric transmission windows around the 2.05-µm wavelength. The LO is connected to the fiber network, which is configured to divide and distribute LO light to four heterodyne detectors: the atmospheric channel 50/50 coupler (see LPM), the reference monitor detector, and the two offset lock circuits. LO polarization on the outgoing atmospheric channel fiber branch must be set to S- or P- to match the selected transmit laser polarization. A compact fiber-coupled low-voltage Pockels cell performs this function as specified by the lidar control system. A fraction of the outgoing laser pulse is mixed with the LO in a coupler and sent to the reference monitor detector, generating an IF signal digitized by the Science Data Acquisition System. The monitor signal data captures transmit laser pulse strength and frequency for every pulse that is required for calculating Doppler shifts of the atmospheric return.

Two Swift lasers are configured as tunable MO references. A programmable, feedback controlled, offset lock circuit precisely sets MO frequency at a specified offset from the LO. A heterodyne detector generates an IF beat signal proportional to the LO-MO frequency offset, which can range from 150 MHz to 4 GHz. The offset is selected to compensate for spacecraft/aircraft platform velocity-induced Doppler shift such that zero wind speed is centered (135 MHz) within the receiver electronic bandwidth (25-245 MHz). The optical frequency of MO1 is normally above the LO frequency, and MO2 is below. The dual MO architecture was designed to enable wind measurement in the forward and aft directions relative to orbital platform motion. The locked MO1 and MO2 outputs are fed into an optical switch, which selects the MO commanded by the lidar system controller to seed the transmit laser with the desired wavelength.

For an orbital mission, the time of flight for light to travel from a satellite orbiting at 400 km (457 km slant path range at 30° off-nadir angle) to the surface and back is ~3 milliseconds (ms). The RMS frequency variation of the LO over 3 ms is < 50 kHz which translates into only a 5.1 cm/s RMS velocity error. This is more than sufficient for atmospheric wind measurement applications. Transmitted pulse frequency variations due to shot-to-shot jitter, MO aging, and other potential causes are precisely measured. Due to precise offset frequency locking the frequency variations in the offset-locked MO lasers follow closely that of the LO. It is important to note that since the frequency of the outgoing pulses is measured by the monitor detector the frequency stability of the MO is not very critical. To ensure that all Doppler-shifted transmitted frequencies stay within high-transmission atmospheric windows, the LO is specified with no more than +/- 5 GHz (+/- 70 pm) frequency drift from 2052.92 nm over its lifetime.

2.5. Auto-Alignment System (AA)

AWP has two critical alignments: the transmit laser oscillator cavity and the Tx/Rx beam overlap. CDWL has stringent demands on optical alignment stability. A two-channel AA system was designed and incorporated into AWP to optimize and maintain oscillator performance and Tx/Rx overlap. The oscillator mirrors are mounted in athermal Invar mounts which are mounted onto an athermal CFC optical bench. Even though the mirror mounts and underlying bench are stable, small thermal- or shock-induced misalignments can still occur due to the long-folded cavity with its

https://doi.org/10.5194/egusphere-2026-4872
Preprint. Discussion started: 19 August 2026

eight cavity mirrors. To correct for such misalignments, an actuated angle-adjustable mirror is included in the oscillator. The oscillator energy monitor measures peak and baseline oscillator output. An intracavity mirror is mounted on a motorized tip-tilt mount with inductive position feedback on both axes (Osc AA in Figure 2). The AA controller analyzes the signal via commanding several minor angle displacements from the current angle, using measurements at these points to determine the gradient of the energy profile, and reorients that cavity mirror accordingly to maximize energy output.

The Tx/Rx alignment system aligns the transmitter beam to the receiver field of view. A small portion of the P-polarized beam is allowed to leak through a mirror, which passes through a far-field imaging lens onto a quad cell detector. The four quad cell channels are digitized, indicating position of the transmit beam path. A 1.55 µm back-propagating local oscillator (BPLO, located in the LPM) is coupled into the receiver optical path through the WDM. A WDM allows joining or splitting different wavelengths of light to and from a single fiber. As configured with AWP, the WDM passes 2 µm light from the common fiber to the 2 µm output fiber, and 1.55 µm light passes from the BPLO fiber to the common fiber. In this configuration, the BPLO exactly indicates the receiver axis. The BPLO light is reflected off a mirror mounted on a motorized tip-tilt mount with inductive position feedback on both axes (Rx AA in Figure 2). The reflected light passes through the same mirror and lens as the P-polarized beam, landing on the same quad cell. The transmit laser and BPLO alternate pulses, allowing the quad cell to capture both spot positions. The near-field beams in the HPM are transformed into the far field using a transform lens. The AA controller utilizes this quad cell data to determine the relative positions of the far field beams, and autonomously commands the Rx AA mount to move the receiver view angle as needed to overlap the transmit beam in the far field. The Tx/Rx AA system is also designed to correct lag angle misalignments, allowing for receiver alignment maintenance even in the presence of a rotating LOS due to satellite orbit rotation. Lag angle correction is achieved by precisely pointing the beam at some fixed offset angle from the transmit beam.

2.6. Beam Expanding Telescopes

Being a monostatic lidar, the atmospheric backscatter signal returns to AWP through the same telescope of the transmitted pulse. Two nominally identical, mostly aluminum telescopes are installed in AWP for each beam path. Both telescopes have a 20x expansion ratio, expanding the beam from 6 mm to 120 mm diameter (e^{-2} intensity) for transmitted pulse, then similarly compressing the backscattered return signal. The telescopes have a 150 mm diameter clear aperture and filling this aperture with a Gaussian beam with 120 mm diameter results in the highest CDWL antenna efficiency (Wang, 1988; Henderson, 2005). The telescopes have a four-mirror, off-axis, f/8 Cassegrain design, folded to each occupy a volume of approximately 34 cm x 36 cm x 19 cm (Figure 5). The large primary and secondary mirrors (M1 and M2) use a nickel-plated aluminum substrate with a protected gold optical surface. M3 is a fused silica element with a protected gold coating, and M4 is a calcium-fluoride (CaF) element, with a dielectric reflective coating. As initially delivered by the vendor, the telescopes were poorly aligned, achieving at best λ/3 (RMS) wavefront error at 633 nm, or approximately λ/9.5 (RMS) at 2.053 µm, resulting in an estimated antenna efficiency loss of ~10 dB. Maintaining low wavefront error is particularly important for coherent detection lidar systems (Rye 1982; Henderson et al. 2018a). After realignment at LaRC in 2024 to address significant signal loss encountered in 2023 AWP flights

https://doi.org/10.5194/egusphere-2026-4872
Preprint. Discussion started: 19 August 2026

(Bedka et al. 2024), they achieved a transmitted wavefront error of better than λ/20 (RMS) at 2.053 μm which results in < 0.5 dB loss in the lidar antenna efficiency compared to perfect optics.

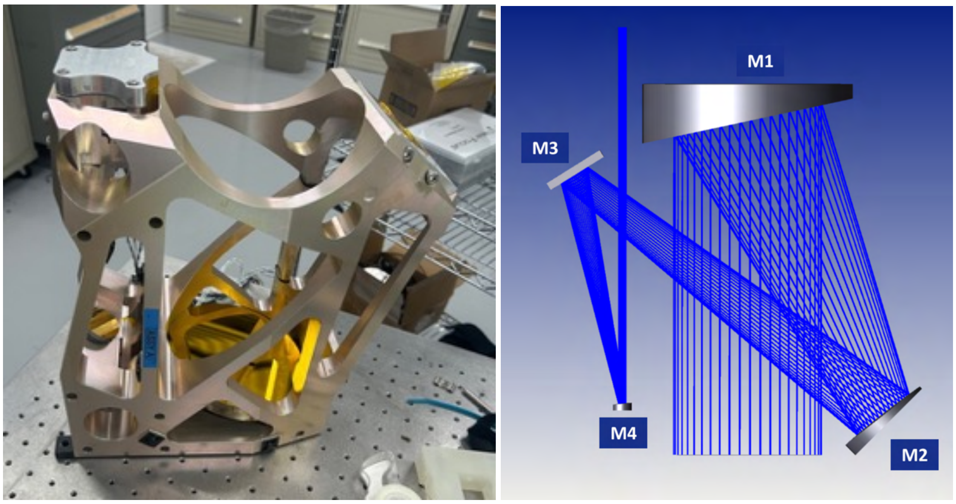

Figure 5: (left) An AWP beam expanding telescope, photographed while sitting up-side down in a LaRC laboratory. The 15 cm diameter primary mirror (M1) with gold coloring is located at the bottom of the telescope. The expanded beam would leave the AWP instrument and be transmitted into the atmosphere through the circular opening at the top. (right) A diagram illustrating beam expansion by the four-mirror system.

2.7. Beam Steering Assembly

AWP beam steering is accomplished by rotation of a symmetric silicon prism. The basic mode of operation for this assembly is start-rotate-stop-sample. The custom rotation stage was designed to complete a 90° rotation in one second, but has been demonstrated to ~350 ms. A brushless DC servo motor is coupled to the rotor through a 5:1 reduction belt drive, and three large-bore bearings support the prism and the rotor components. Silicon was selected for the prism material because of its advantageous index of refraction n=3.4484 at 2.05 μm. The surfaces of the silicon prism have an 11.9° separation angle, resulting in a 30° beam deflection angle (Figure 6-left). Mounting the prism at an angle to the incident transmitted beam both eliminates back-reflections of the high-power laser pulse and maximizes beam quality by eliminating the elliptical distortion (beam compression in one axis) typically generated by a wedge deflector such as that used in the DAWN lidar. Elimination of the beam compression (a.k.a. squint) that occurs in typical wedged scanners is important as the squint results in loss in the lidar antenna efficiency. For DAWN the squint-induced loss is about 1.1 dB. This loss is mitigated in the AWP scanner design. The prism is anti-reflective coated on both surfaces (Figure 6-right), minimizing optical surface losses and balancing any coating-induced stresses on the optical element.

https://doi.org/10.5194/egusphere-2026-4872
Preprint. Discussion started: 19 August 2026

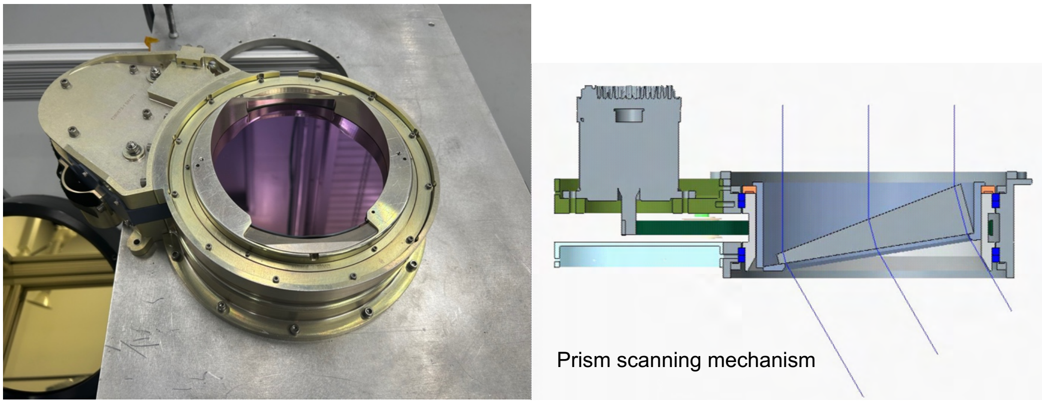

Figure 6: (right) A photo of the underside (opposite of the left panel orientation) of AWP beam steering prism mechanism that would face toward the aircraft window and the atmosphere. (left) A schematic representation of the AWP rotating symmetric silicon beam steering prism mechanism.

3. Data Acquisition and Wind Retrieval Methods

3.1. Scan Strategy

AWP operated with two LOS to enable wind vector measurement during the Fall 2024 flights, oriented at a +/-45° azimuth from the aircraft centerline (Figure 7). The number of pulses per LOS is selectable depending on flight science goals. For its most commonly used operating mode in Fall 2024, AWP emitted a pulse sequence at one LOS ('LOS 1' in Figure 7) for 6 second period, and then the scanner rotated to the other LOS ('LOS 2'). As the scanner rotated between the LOS's, the laser beam was redirected to the nadir telescope typically for a 1-second period. A 6 sec pulse sequence is then generated at LOS 2. This step-stare scan sequence is continuously repeated. To derive a horizontal wind vector, half of the pulse sequence from LOS 1 (3 sec) could be paired with half of the LOS 2 pulse sequence so that all pulse information used in the retrievals is independent. Alternatively, the entire sequence from LOS 1 could be paired with that from LOS 2 to integrate more pulses and improve backscatter sensitivity. In this scenario, data from an LOS is re-used for adjacent wind vector retrievals. In both scenarios, the vector profile is assigned to the coordinate where the LOS switch occurs. As described below, signal from the nadir beam can be included to generate a 3-D wind retrieval. When 1 sec for nadir profiling (the default used for nadir throughout the campaigns) is included, 3-D wind vector profiles are derived at 7 sec intervals, equating to ~1.6-1.8 km spacing assuming a 225-260 m/s airspeed range.

The default 6-second sampling duration per LOS was selected based on experience with AWP upward-looking laboratory testing to provide a balance between aerosol backscatter sensitivity and horizontal spacing between profiles. In practice, an increased number of lidar pulses from the same LOS across multiple scans could be integrated to further improve sensitivity to weak backscatter conditions (as described below), but there would be gaps in the data while the other LOS is being scanned which may not be desirable for some applications. Reduced sampling time at each LOS would reduce such gaps to enable more continuous observations per LOS and flexibility with data integration. But this integration capability across scans was not yet in place in onboard AWP wind retrieval software at the time of the flights, so the decision was made to use longer sampling to maintain better real-time situational awareness of

https://doi.org/10.5194/egusphere-2026-4872
Preprint. Discussion started: 19 August 2026

instrument performance, and the aerosol and wind conditions being sampled.

For an aircraft flying at 12 km altitude, the Earth-intersection of the two LOS beams is ~10 km apart, thus AWP vector wind profiles retrievals represent dynamics from an air volume around the aircraft and not directly beneath it. One alternative would be to scan 5 or more LOS, the scan strategy used with DAWN, to sample both beneath and around the aircraft. This would increase the horizontal spacing between profiles though due to the additional time devoted to sampling three additional LOS. Another alternative would be scanning at 45° and 135° azimuths that would ensure observation of the same atmospheric curtain located ~5 km to the side of the aircraft track at the ground, a concept to be employed in future airborne campaigns and within an orbital DWL mission concept.

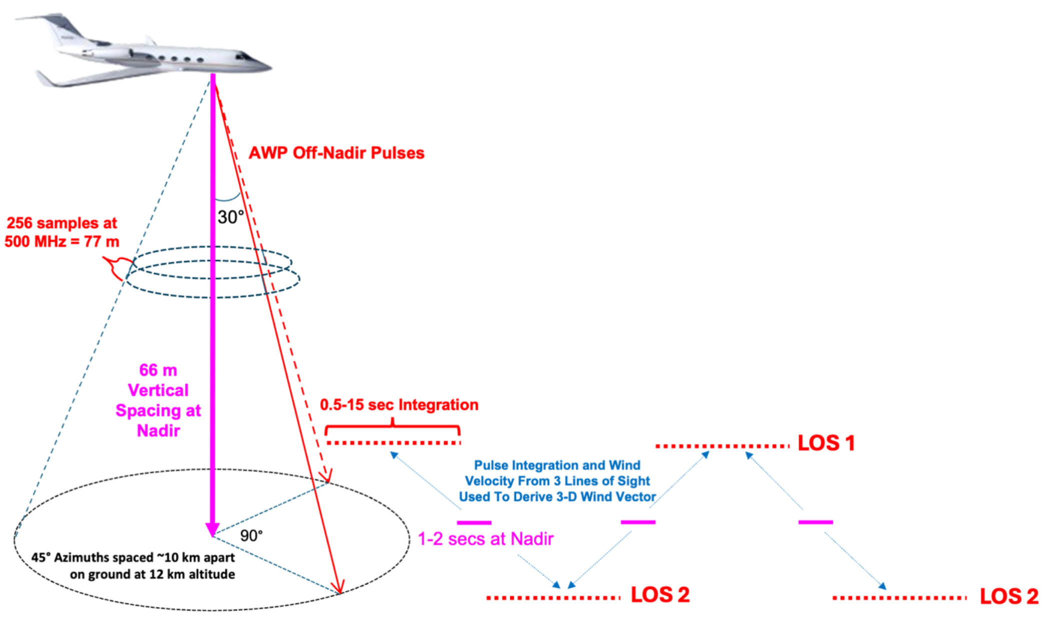

Figure 7: AWP concept of operations for airborne wind vector profiling during the Fall 2024 AWP campaigns.

3.2. Data Collection and Wind Retrieval

After pulse transmission, backscattered light is detected and converted to electrical signals digitized at 500 MSps, with 65528 8-bit data samples stored per pulse in a MySQL database. The sample count and digitization rate provide a slant path range of ~19.6 km or a vertical range of ~17 km. This is sufficient for profiling from most NASA research aircraft, while also providing many samples beneath the surface to compute an instrument noise floor required to derive signal to noise ratio (SNR, see below). After a pulse is transmitted, light reflection from the aircraft window and AWP prism dominates the initial signal return, causing a blind spot between the aircraft and the first valid retrieval bin for the first 4 vertical bins (~264 meters).

The AWP 3-D wind retrieval method is based on Kavaya et al. (2014), initially developed for application with DAWN. Figure 8 provides a flowchart summarizing the retrieval process. Per Kavaya et al. (2014), prior to retrieval, the AWP beam orientations are transformed from an aircraft-relative coordinate to a north-east-down (NED) Earth-

https://doi.org/10.5194/egusphere-2026-4872
Preprint. Discussion started: 19 August 2026

relative coordinate system, incorporating aircraft attitude information from an onboard inertial navigation system (INS) unit. The wind retrieval range resolution is dictated by a combination of the laser pulse duration and the number of data samples used in the wind retrieval calculation. Following Kavaya et al. (2014), the AWP pulse has a duration of 250 ns, corresponding to a 37.5 (32.5) m slant-path (vertical) distance. AWP retrievals are derived from either 256 or 512 data samples per range bin. 256 samples at 500 MSps digitization equates to 76.8 meter slant path range. This becomes 66.5 meters when projected into the vertical, or 133 meters for 512 samples. The vertical spacing between retrieval bins could be set to any user-defined interval, 30 meters for example, which would require more than half the samples to be re-used for adjacent bins.

AWP records two channels of data: 1) samples from the initially transmitted pulse to derive a reference frequency and 2) samples from atmospheric backscatter to derive aerosol backscatter intensity and wind. A Fast Fourier Transform (FFT) is applied to both channels, where 256 (512) data samples are zero padded to achieve a 1024 (2048) sample size for the FFT. The result of the FFT is a periodogram, an estimate of the power spectrum, that is interpolated to 8192 samples to improve precision of the signal peak detection and velocity resolution (~0.03 m/s bin size). Use of a greater number of atmospheric channel samples in the FFT improves sensitivity to weak backscatter (see Figures 12-13) but coarsens range resolution. Every periodogram being integrated per LOS is aligned based on the pulse reference frequency. The Doppler shift induced by aircraft velocity projected onto a LOS, obtained by a dot-product of aircraft airspeed vector and the LOS attitude vector described below, is subtracted. Periodograms from all pulses at an LOS are then averaged at each of the three LOS.

The next step is a search for a signal peak within the averaged periodograms. Selection of a correct peak yields very accurate wind velocities, while selection of a noise peak results in a random velocity. The frequency at the peak is the key piece of information used to derive a Doppler shift from aerosol motion. From the periodogram, two metrics of backscattered signal power can be derived, the SNR and carrier-to-noise ratio (CNR). The carrier to noise ratio is $\mathrm{CNR} = S/\mu$ where S is the mean signal power and μ is the mean noise floor power (Figure 9-left). The other is SNR $= S/\sigma$, where σ is the variance of the noise floor after pulse averaging. SNR indicates how strong a signal peak is relative to noise floor fluctuations. σ and μ is derived from averaged periodograms from samples from below the ground/ocean surface, where the signal return is entirely noise. The averaged periodograms for each vertical bin as a function of frequency are normalized by the noise floor: $Spectrum_{norm}(freq) = (Spectrum(freq) - \mu) / \mu$.
The standard deviation is also normalized: $\sigma_{norm}(freq) = \sigma(freq) / \mu(freq)$.
The peak S is detected in each altitude bin as the largest $Spectrum_{norm}(freq)$ within the search window bandwidth (see below). SNR is defined as $SNR(altitude) = S(altitude) / \sigma_{norm}(freq\_max)$ where $freq\_max$ is the frequency index of the peak. We express SNR as the ratio above in this paper, but one can also express SNR in decibels via $10*\log_{10}(S/\sigma)$.

A depiction of μ and σ as a function of pulse integration, measured during laboratory testing, is provided in Figure 9-middle and -right panels. The μ is has a downward slope with increasing frequency due to an operational amplifier in the dual-balanced receiver. After 100 pulse integration, the noise floor shape remains quite consistent. A local noise spike at 163 MHz indicates the LO frequency assigned during this test. σ decreases by 15x with increasing integration, enabling detection of smaller amplitude aerosol signal peaks as discussed below. σ generally follows the relation $1/2*\sqrt{N}$, indicating that AWP receiver noise is normally distributed. Periodograms from a single AWP LOS profile

https://doi.org/10.5194/egusphere-2026-4872
Preprint. Discussion started: 19 August 2026

during transit flight from Moffet Field, CA to Hampton, VA on 15 November 2024, which featured AWP dwells for 15 seconds per LOS, demonstrate the impact of increasing pulse integration on S (Figure 10). A reduction in speckle return via integration enhances S and deepens the atmospheric layer where a signal peak can be reliably detected. This reinforces the utility of adaptive integration for signal detection in weak backscatter conditions (Frehlich et al. 1997; Frehlich 2004). Given the continued reduction in σ from 3000 pulses to 12000 pulses (Figure 9), and the emergence of a diffuse aerosol layer at a ~5-8 km altitude with 3000 pulses in Figure 10, it is possible that a detectable signal peak would be present throughout a greater fraction of the column if AWP were to have dwelled longer per LOS. Increased pulse energy would also increase signal intensity, requiring shorter integrations.

The fraction of errant peak detections is a function of SNR and the bandwidth of the search window (Frehlich 2004; Henderson et al. 2018b). We search over a selectable bandwidth relative to the reference frequency and set a SNR detection threshold at 2.8σ (3σ) for the off-nadir (nadir) beams. A smoothed 2-D periodogram image is analyzed to trace the frequency position of most likely peaks to identify the search window bandwidth for the entire profile. The nadir threshold is set slightly higher because of the much shorter (1 sec) dwell time for nadir relative to off-nadir, and the desire to achieve the most accurate vertical motions enabled by more prominent peaks. Reducing thresholds will increase retrieval success rate, but will also increase errant peak detections, so these thresholds were found to be a good compromise after experimentation. After averaging to reduce speckle fluctuation of the signal, the peak amplitude S is dominated by aerosol backscatter intensity, but is also modulated by the wind speed variance in the range bin being sampled. Greater variance (i.e. turbulence) will disperse the peak across multiple frequency bins and decrease the SNR.

Because the AWP range bin size (76.8 meters) is relatively large compared to surface topography variations that can be present across the integrated data duration, the non-moving ground can bias wind retrievals in the lowest atmospheric data bin, so it is important to take special considerations for near-surface retrieval. The intersection of an LOS with the surface is initially estimated from the NOAA 30 arc-second ETOPO Global Relief Model (NOAA NCEI, 2022). Four bins between five levels closest to the predicted surface elevations are defined, with the lowest level residing at the surface. Four bins are then expanded to 16 bins (~5 meter spacing) and atmospheric samples are assigned to each bin. SNR profiles are derived along this fine-scale grid, and analyzed from the top to bottom altitude where a vertical running mean of SNR is derived. When the mean SNR at a bin is double the running mean, it is assumed that this bin influenced by the surface. The wind profile is set to the first valid retrieval above surface beneath the lidar-estimated surface.

Aircraft attitude uncertainty, as well as uncertainty of the true orientation of AWP relative to the aircraft centerline, can lead to non-zero speed being retrieved at the surface and throughout the profile. Precise attitude measurement and instrument orientation knowledge is critically important for nadir beam vertical motion retrievals, where motions are typically +/- 1 m/s. The aircraft is moving at 200+ m/s, so attitude uncertainty can lead inaccurate projection of aircraft motion component onto an LOS, and significant inaccuracy in vertical motion. To quantify uncertainty, wind speed from both the off-nadir and nadir beams is analyzed at the identified land surface for many flight segments over flat land distributed across several flights. Attitude uncertainty, especially for aircraft yaw, was evident based on comparison of data from three INS/GPS measurement units aboard the G-3, while measured

https://doi.org/10.5194/egusphere-2026-4872
Preprint. Discussion started: 19 August 2026

airspeeds between the units were in very close agreement. The AWP INS/GPS unit, from which data is synced with each 200 Hz laser pulse, produced unreliable yaw measurements throughout the Fall 2024 campaigns, requiring use of a 10 Hz yaw measurement from another onboard unit. All other aircraft state measurements used in the retrieval were from the 200 Hz AWP unit. Attitude parameters were iteratively analyzed to find the combination that yielded mean speed and variance closest to zero for both nadir and off-nadir beams (not shown). The offset uncertainties required to achieve zero ground velocity from flight to flight caused yielded surface wind speed uncertainty of < 0.1 m/s, which we define as the AWP vertical wind measurement uncertainty.

LOS-relative wind speed V_{LOS} is calculated as:

$$V_{LOS} = (\,Signal\ Peak\ Frequency\ -\ Reference\ Frequency\,)\frac{\lambda}{2}$$

where λ is the laser wavelength. The desired 3-D wind vector $\vec{W}$ can be expressed in the NED coordinate system with (W_N, W_E, W_D) components. Projection of $\vec{W}$ onto a LOS described by a attitude vector $\vec{u}$ is given by:

$$V_{LOS} = \vec{u} \cdot \vec{W}$$

Each of the three LOS atttiude vectors is described by the beam polar elevation angle θ_i and azimuthal angle ψ_i (i=1, 2, 3), and so the following linear system can be composed:

$$\begin{pmatrix} \sin\theta_1 \cos\psi_1 & \sin\theta_1 \sin\psi_1 & \cos\psi_1 \\ \sin\theta_2 \cos\psi_2 & \sin\theta_2 \sin\psi_2 & \cos\psi_2 \\ \sin\theta_3 \cos\psi_3 & \sin\theta_3 \sin\psi_3 & \cos\psi_3 \end{pmatrix} \begin{pmatrix} W_N \\ W_E \\ W_D \end{pmatrix} = \begin{pmatrix} V_{LOS1} \\ V_{LOS2} \\ V_{LOS3} \end{pmatrix}$$

Since our three attitude vectors (one nadir beam and two off-nadir azimuthal beams) are not coplanar, they are linearly independent and form the basis of a 3-D space. Therefore, the coefficient matrix above is invertible, and the linear system is well-posed with a unique solution. This yields the three components of the wind vector, as long as all three LOS have sufficient SNR. If a peak within the nadir beam signal cannot be detected reliably, then the system above can be reduced to a 2-dimensional version that yields a solution for the two horizontal wind components. Given that nadir sampling was typically 1-second duration, relative to 6-second sampling per off-nadir LOS, nadir beam peaks are not as prominent and therefore 3-D wind retrieval is only done for the subset of vertical bins with sufficient nadir beam return. If signal is insufficient with 256 samples, another retrieval attempt is done with 512 sample / 133 m processing, where successful retrievals are duplicated to 66 m bins. Profiles with aircraft roll ≥ 2°, indicating an aircraft turn and non-constant dwell at a particular azimuth, are omitted.

Figure 11 shows SNR and horizontal wind speed retrieval curtains throughout the 15 November flight. With 50 pulses, wind retrievals are limited to the PBL, clouds, and other strong backscatter regions especially near to the aircraft. The SNR and wind retrievals are consistent with observed HALO 532 nm backscatter patterns (lower-left) with 600 pulses. Additional integration with 3000 pulses fills more of the mid-tropospheric signal gap during the second half of the flight, yielding wind retrievals where HALO backscatter is near to or beyond the minimum threshold required for quantitative aerosol intensive property retrieval. Further analysis of the 15 November 1935 UTC profile discussed in Figs. 10-11 shows that successful peak detection and wind retrieval increased from 19% of the atmospheric column with 50 pulse integration to 78% with 3000 pulse integration and 256 sample FFT processing. Increasing to 512 FFT processing increased success rate by an additional 8% (not shown). Retrievals were successful at the highest vertical resolution for the vast majority of the flight but, as discussed above, 512 sample integration was

https://doi.org/10.5194/egusphere-2026-4872
Preprint. Discussion started: 19 August 2026

required in weak backscatter conditions primarily in the middle altitudes of the curtain.

AWP data products currently include horizontal wind speed and direction, vertical wind speed, and SNR profiles. Speed and direction are converted to U- and V-components for the convenience of the user. A spatio-temporal smoothed horizontal wind speed/direction and wind components product is also included. This product is intended to remove small scale variability of the winds that may be detrimental for NWP data assimilation, and fill in gaps across brief aircraft turns. AWP data are weighted-averaged over a 150-sec time window, encompassing a 34-km distance assuming a 225 m/s ground speed, as well as 5 AWP vertical bins (330 m). The profile at the center of the window is weighted highest, and the weighting linearly drops off to zero at the window edges. Aircraft attitude and velocity, the vertical integration used (66-133 meters) to achieve a successful retrieval, the lidar detected land surface elevation, the maximum ETOPO30 land surface elevation across the 3 AWP beam positions, and other ancillary parameters are also included.

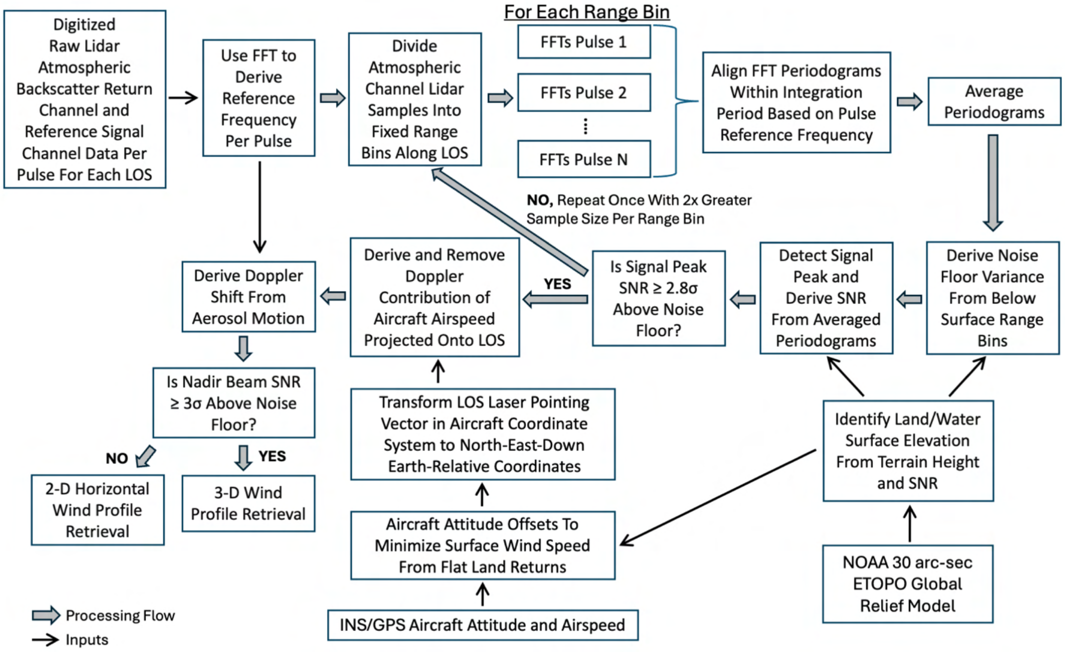

Figure 8: A flowchart summarizing the AWP 3-D wind retrieval process

https://doi.org/10.5194/egusphere-2026-4872
Preprint. Discussion started: 19 August 2026

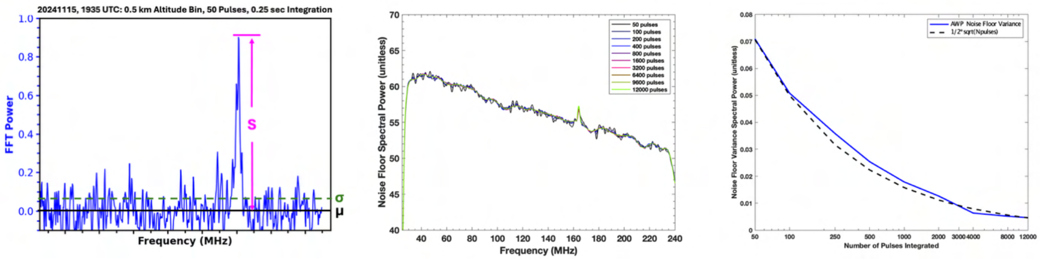

Figure 9: (left) An FFT periodogram from a 0.5 km altitude bin from 15 November 2024 at 1935 UTC, annotated with spectral signal power amplitude S, mean noise floor μ and noise standard deviation σ. (middle) AWP μ and (right) σ as a function of lidar pulse integration measured during AWP laboratory testing, overlaid with the $1/2*\sqrt{N_{pulses}}$ curve. The noise spike at 163 MHz is the local oscillator frequency.

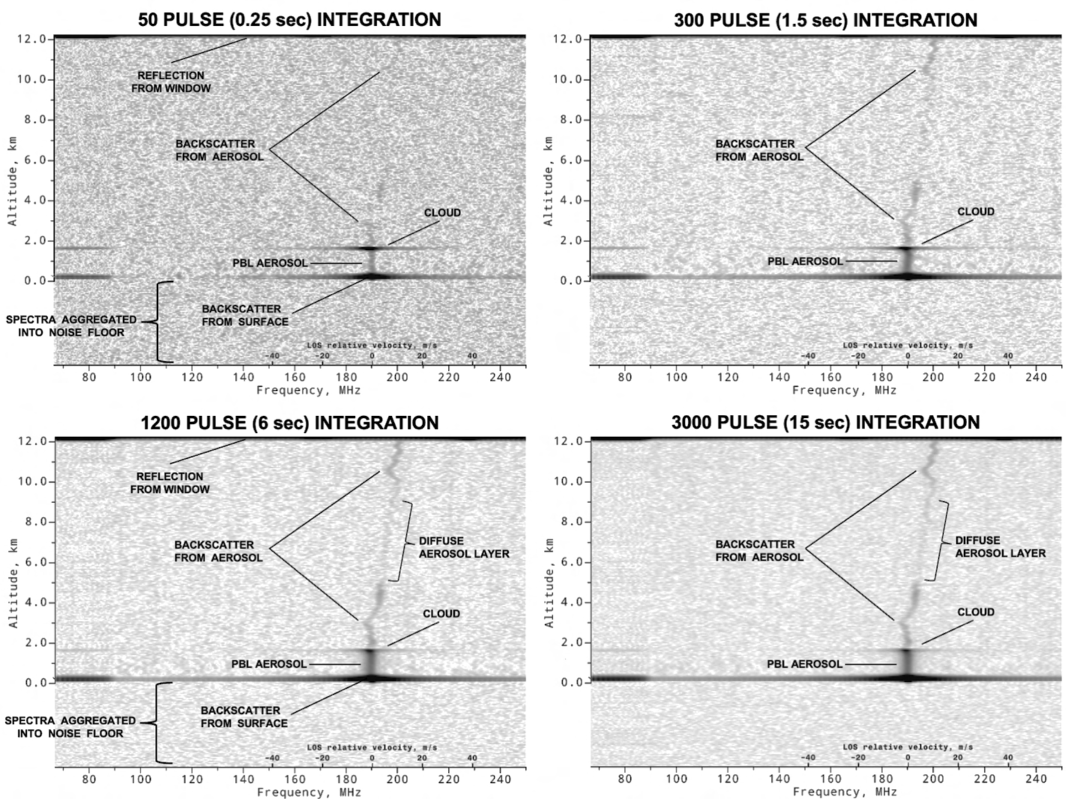

Figure 10: AWP averaged periodograms compiled from a single LOS for a profile at 1935 UTC on 15 November 2024, where both strong and weak backscatter conditions were present. Periodograms are shown with varying pulse integration, and annotated to describe the signals being depicted. Lighter shading indicates a reduced instrument noise through longer integration.

https://doi.org/10.5194/egusphere-2026-4872
Preprint. Discussion started: 19 August 2026

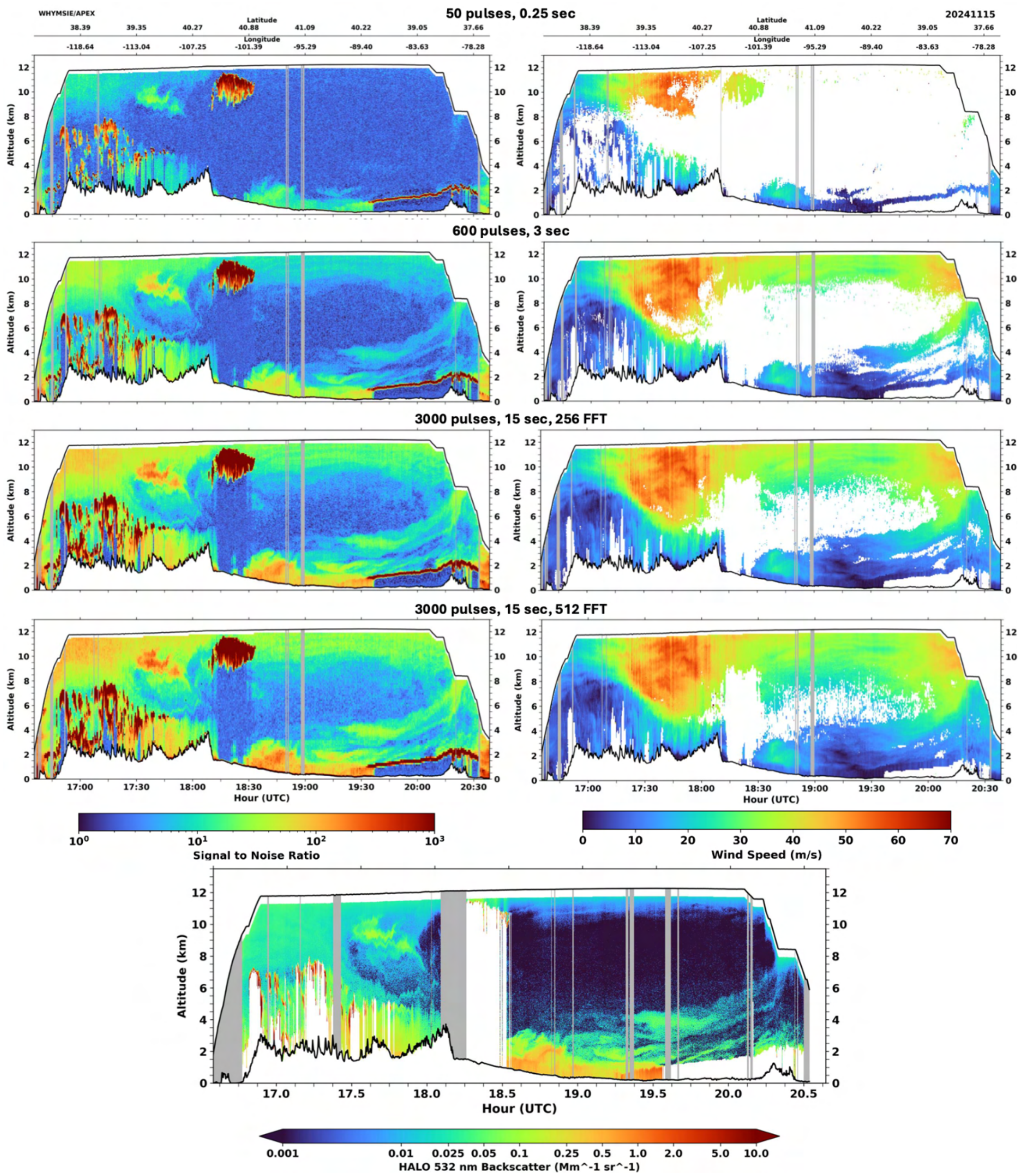

Figure 11: (Top four rows) AWP SNR (left) and wind speed (right) curtains for a flight on 15 November 2025, a transit from Moffett Field, CA to Hampton, VA, using increasing pulse integration duration from 0.25 to 15 sec. (Bottom) HALO cloud-screened 532 nm aerosol backscatter. Grey indicates sharp turns or periods during flight where HALO was not operating, and white indicates areas beneath opaque cloud.

https://doi.org/10.5194/egusphere-2026-4872
Preprint. Discussion started: 19 August 2026

4. Example AWP Flight Data

A flight on 15 October 2024 focused on sampling an upper-tropospheric trough depicted by the NOAA Global Forecast System (GFS) over the northeast U.S. and southern Canada (Figure 12). A jet steam with winds exceeding 50 m/s was forecast along the southern edge of the trough and the oceanic portion of the flight track, while < 10 m/s speed was forecast at 250 hPa (~10 km altitude) along the trough axis over southern Ontario. This day featured one of the first infiltrations of a cool Canadian airmass in Fall 2024 over the flight domain, which triggered the formation of widespread cumulus cloud cover (Figure 13-top).

The flight began by heading east from Hampton, Virginia and then northeastward to the Massachusetts coast along the jet stream where which six dropsondes were released. Dropsonde releases were not permitted over land, so validation was limited to this relatively short oceanic flight segment. 50+ m/s wind flow with south-westerly to westerly direction was observed by AWP (Figure 14) which extended down to nearly 6 km altitude (Figure 14). The AWP SNR curtain (Figure 13-bottom) shows that these optically-thick cumulus had SNR in the 300-3000 (24.8-34.8 dB) range and cloud tops between 1-2 km altitude, with occasional penetrations to 3-4 km. AWP's fine spacing between profiles enabled frequent penetration and wind profiling through gaps in the cumulus. The vertical wind speed curtain shows turbulence in the lowest kilometer within or near to the PBL with speeds occasionally exceeding 1 m/s. Above 10 km, several vertically oriented velocity peaks between 17-17.5 UTC are evident. A close examination of both the horizontal wind speed and direction curtain indicates subtle undulations and variability in association with these peaks, but no evidence of perturbations to the SNR curtain.

From 1740-1950 (17.66-19.83) UTC, the flight progressed westward from Massachusetts through the trough axis to near Milwaukee, Wisconsin. The weak jet stream wind flow forecasted by GFS along the trough axis was confirmed by ≤ 5 m/s AWP wind speed observations. AWP SNR shows complex aerosol layering above the cumulus with embedded "clean" regions having very weak backscatter most frequently within 2-3 km of cloud tops which occasionally was insufficient for wind retrieval. A vertical tilt in the structure of the trough caused a mid- to -upper-tropospheric wind maximum to emerge between 19 and 20 UTC. Cirrus and altostratus were present at various times during this flight segment that were often penetrated by AWP to reveal a layer of lower-altitude cumulus. There is a clear SNR gradient around 8 km, with notably higher SNR (green/yellow shading) above 8 km. The GFS model identified the tropopause to be between 7 and 9 km during this east-west flight segment (dashed line), and therefore this enhanced aerosol layer resided in the stratosphere (Figure 13-bottom). Layered, quasi-horizontal wind speed and direction variations are evident in the AWP curtain from 1830-2030 (18.5-20.5) UTC (Figures 15 and 17) within the stratosphere. Spacing between local speed maxima and minima within these structures are found to be ~250 m in some locations. The aerosol distribution depicted by SNR do not appear to be perturbed in the same way as the wind profiles. The physical process causing these layered patterns is unclear and requires further investigation, but given their spacing, high vertical resolution and precise wind profiling capability like that of AWP is required to observe such features.

The vertical wind speed curtain during the 17.66-19.83 UTC timeframe shows several interesting features. Vertical speed was predominantly downward within clouds in the 4-8 km layer, occasionally reaching -1 m/s and attributed to falling hydrometeors. The most significant variations, located within the ~5-12 km altitude layer, occurred

https://doi.org/10.5194/egusphere-2026-4872
Preprint. Discussion started: 19 August 2026

from 18-18.6 UTC (1800-1836 UTC) which were strongest across Massachusetts but also extending eastern New York as the aircraft was transitioning from the jet streak into the trough axis. Subtle undulations of the horizontal winds are also evident in this timeframe (Figure 16). GOES-16 6.2 µm water vapor imagery shows the presence of mountain waves along flight track (Figure 15, Uhlenbrock et al. 2007; Feltz et al. 2009). Mountain wave-induced perturbations to horizontal wind speed had been previously observed by AWP in January 2023 over Virginia (Bedka et al. 2024) and by DAWN in April 2019 offshore of southern California (Bedka et al. 2021). But there does not appear to be any vertical wind variations correlated with the layered quasi-horizontal wind patterns discussed above. The characteristics of the vertical wind differed above and below the tropopause near 8 km, where the region above-tropopause featured vertically-oriented velocity structures while the region below had much more random velocity with the exception of cloudy and mountain wave regions.

The flight then headed southeast through the base of the trough to the Nashville, Tennessee area, and later eastward toward Hampton within the jet stream. Wind speeds at 250 hPa were depicted by the GFS to be highest along this segment, which was confirmed by AWP 60+ m/s observations in the 8-10 km layer. An altostratus layer was present beneath the jet after 2030 UTC across Kentucky, Tennessee and Virginia with tops in the 5-6 km range. Their cloud tops were less opaque than the low-altitude cumulus earlier in the flight, enabling lidar penetration 3+ km into cloud in some instances. Vertical motions were neutral to slightly upward within these cloud tops, but typically downward beneath the tops suggestive of falling hydrometeors. Mountain waves were evident in the SNR curtain during aircraft descent near the end of the flight on the eastern side of high elevations of the Appalachians. Horizontal wind speed varied by several m/s from mountain wave peak to trough, while vertical motions exceeded +/- 1 m/s which extended up to the ~10 km aircraft altitude. GOES-16 water vapor imagery also showed mountain waves in this region, though they were more subtle than those in Massachusetts and New York earlier in the flight (Figure 15).

AWP had excellent agreement with Airborne Vertical Atmospheric Profiling System (AVAPS) dropsondes (NSF NCAR, 1993) during this flight (Figure 17). The AWP winds (red) often directly overlaid the sonde (black) profiles. Differences were greatest below 3 km altitude including within the PBL. These differences are attributed to the fact that there was considerable sonde drift (20+ km) away from flight track by the time the sondes reached ≤ 3 km altitude due to strong jet stream flow, and winds within/above the PBL are typically more spatially variable than winds aloft. AWP yielded successful wind retrievals for nearly the entirety of the AVAPS-colocated profiles due to strong backscatter throughout the column. Part II of this paper features quantitative AWP-AVAPS comparisons including 68 dropsondes released throughout the Fall 2024 campaigns that further demonstrate AWP's high accuracy and precision (.09 m/s bias, 0.90 m/s root-mean-squared difference).

Given the strong AWP agreement with dropsonde, AWP data can be used as a reference to assess the performance of NWP models or other wind estimates such as those from GOES AMVs. Figure 18 shows AWP data wind speed and direction retrievals averaged to the 0.25° GFS model resolution, GFS model wind analyses time interpolated to the AWP data, and the difference between the averaged AWP and GFS winds along the G-3 flight track for the same 15 October flight discussed above. There is good qualitative agreement between the AWP and GFS datasets, where the key jet stream features and trough position are depicted well by the GFS. The primary differences were located around the mid- to upper-tropospheric wind speed maximum between 19-20 UTC and along the lower edge of the

https://doi.org/10.5194/egusphere-2026-4872
Preprint. Discussion started: 19 August 2026

second encounter of the jet stream near the end of the flight. Additional comparisons between AWP and GFS model analyses and forecasts are shown in Part II of this paper, where differences are more comprehensively quantified.

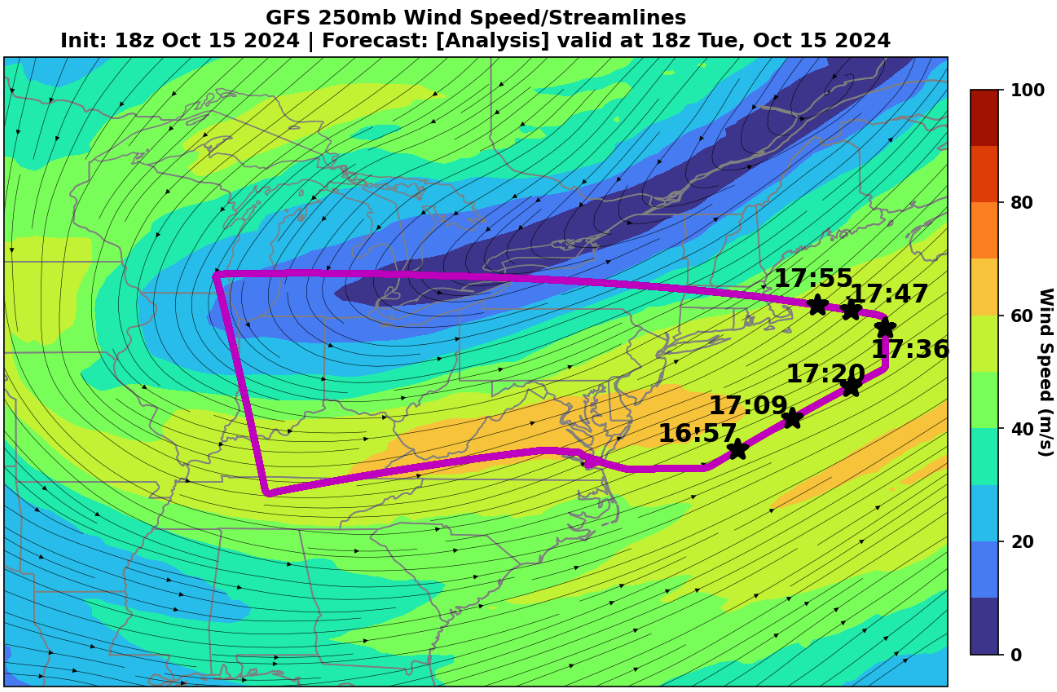

Figure 12: NOAA Global Forecast System (GFS) 250 hPa wind analysis valid at 18 UTC on 15 October 2024, overlaid with the G-3 flight track (magenta) and dropsonde release locations/times (black stars/text).

https://doi.org/10.5194/egusphere-2026-4872
Preprint. Discussion started: 19 August 2026

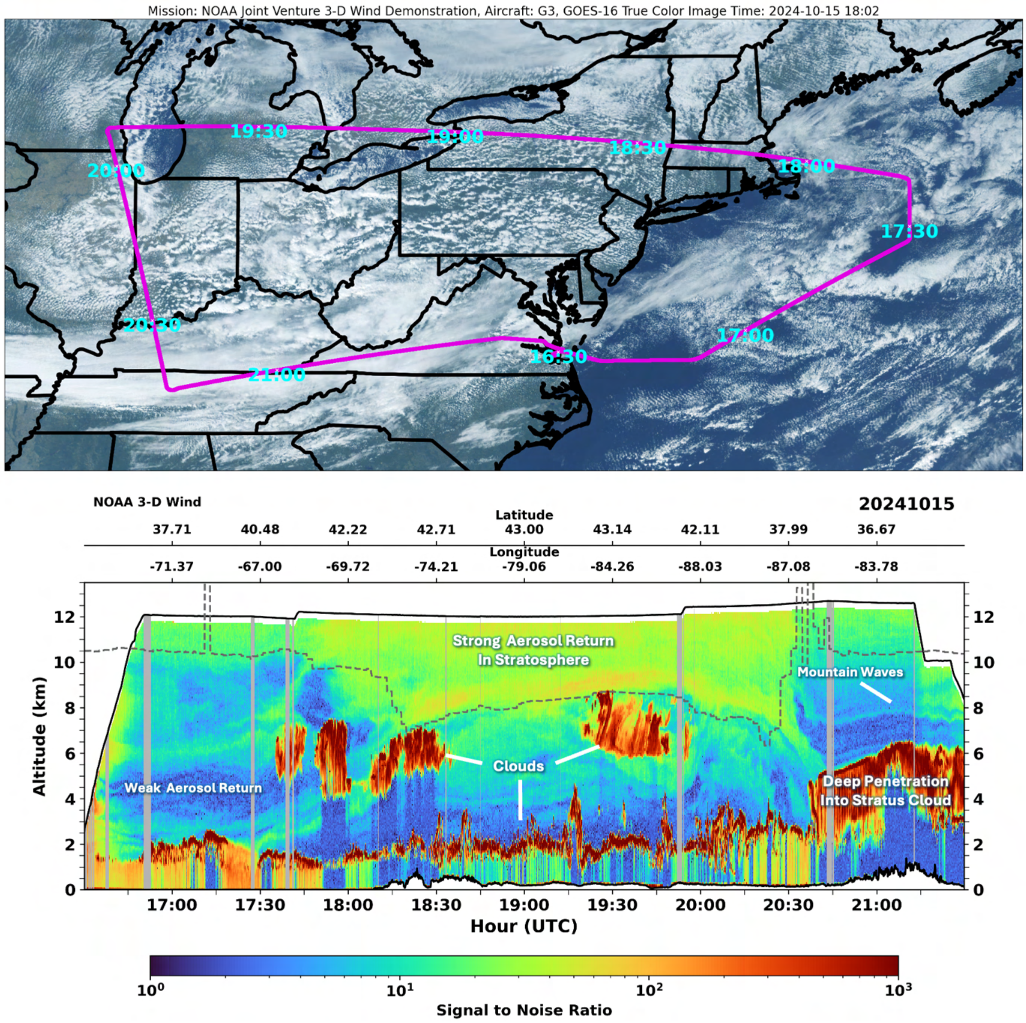

Figure 13: (top) GOES-16 True Color RGB composite on 15 October 2024 at 1802 UTC, overlaid with the G-3 flight track (magenta) and flight time in UTC (cyan). (bottom) AWP signal to noise ratio (SNR). White columns in the curtains indicate aircraft turns where wind profiles are invalid. The dashed line is the Global Forecast System (GFS) tropopause height analysis along flight track. Annotations indicate various features discussed in the text.

https://doi.org/10.5194/egusphere-2026-4872
Preprint. Discussion started: 19 August 2026

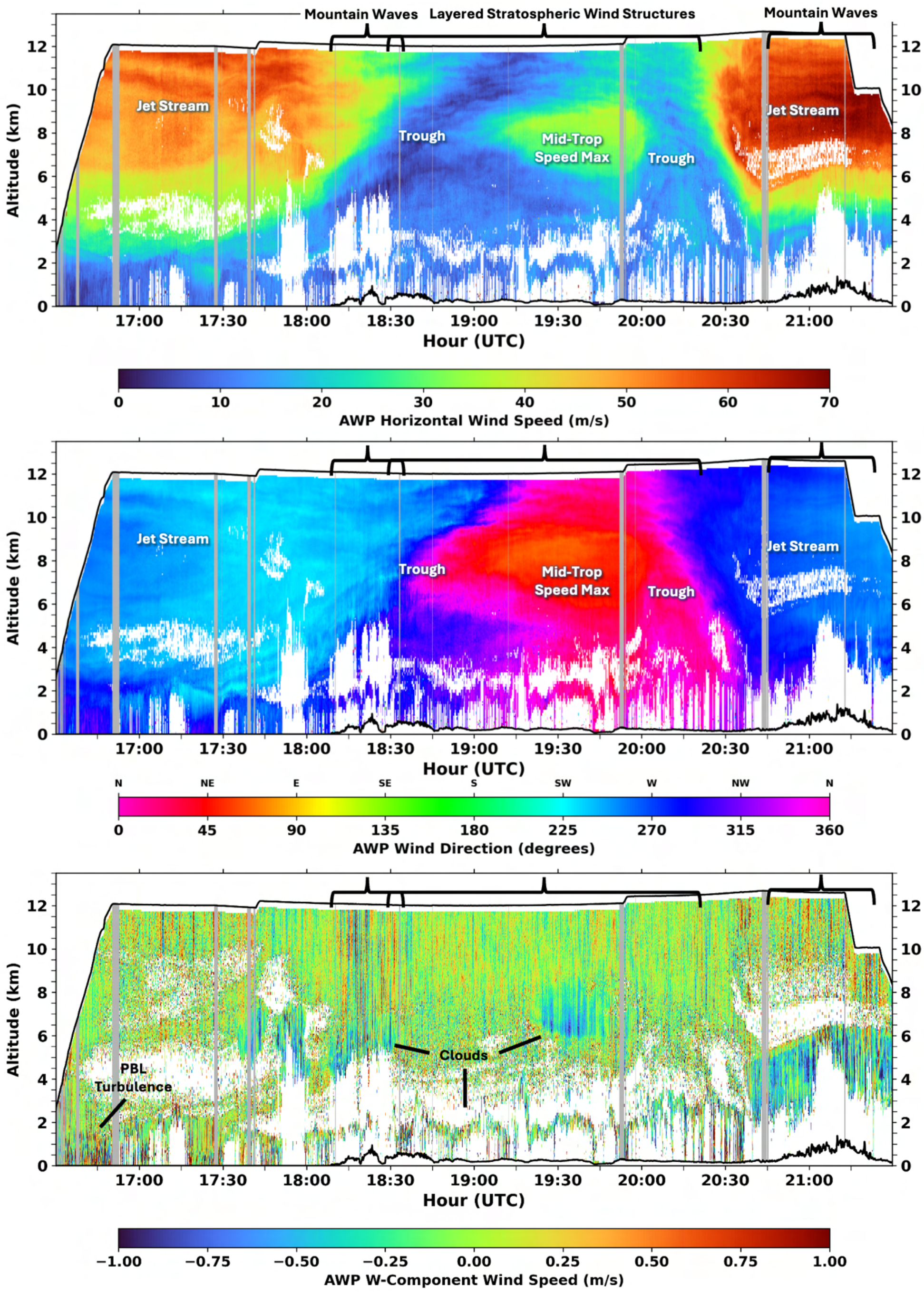

Figure 14: AWP horizontal wind speed (top) and wind direction (middle), and vertical wind speed (bottom) on 15 October 2024. Grey columns in the curtains indicate aircraft turns where wind profiles are invalid. White indicates insufficient backscatter signal for wind retrieval. Negative vertical motions are downward toward the ground.

https://doi.org/10.5194/egusphere-2026-4872
Preprint. Discussion started: 19 August 2026

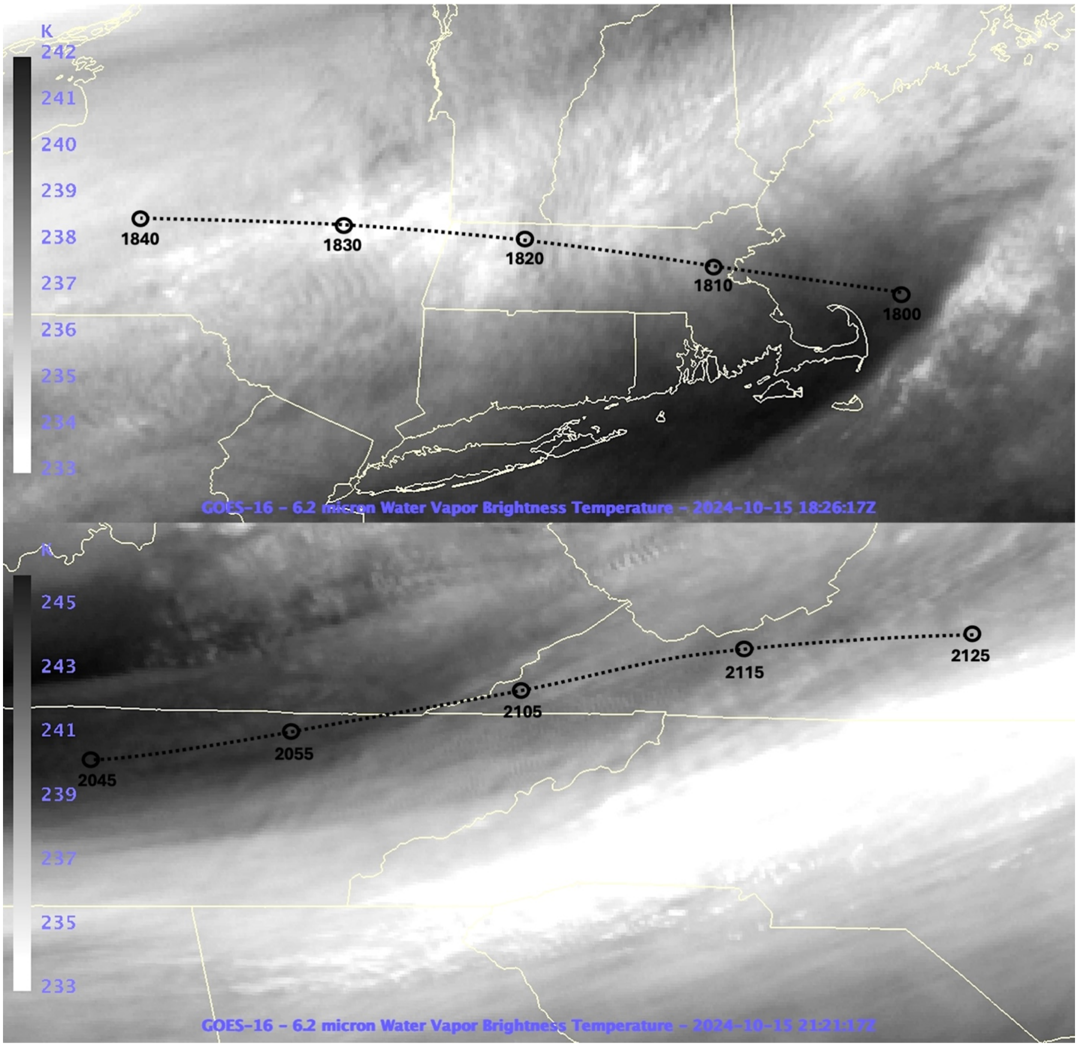

Figure 15: GOES-16 6.2 µm water vapor absorption band imagery at 18:26 UTC (top) and 21:21 UTC (bottom) overlaid with the G-3 flight track, annotated at 10 min intervals. These images indicate the presence of mountain waves that generated 1+ m/s vertical motions observed by AWP.

https://doi.org/10.5194/egusphere-2026-4872
Preprint. Discussion started: 19 August 2026

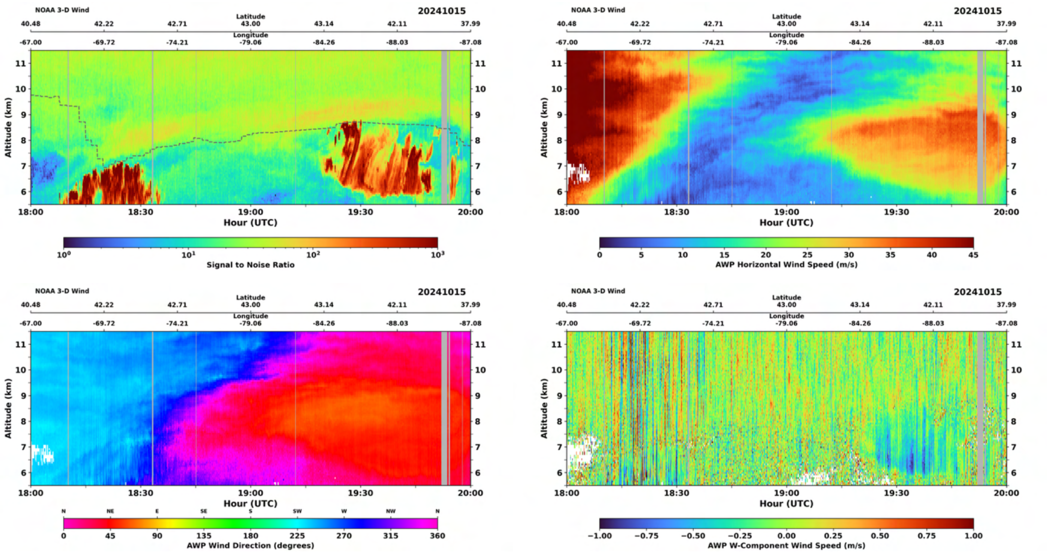

Figure 16: AWP SNR (upper-left), horizontal wind speed (upper-right) and wind direction (lower-left), and vertical motion (lower-right) curtains on 15 October 2024 between 5.5 and 11.5 km altitude where horizontally-oriented wave-like wind variations, and enhanced vertical motions from mountain waves are evident. The SNR and horizontal wind speed color bars are compressed relative to Figure 14-15 to better depict these variations. The dashed line on the SNR curtain is the Global Forecast System (GFS) tropopause height analysis.

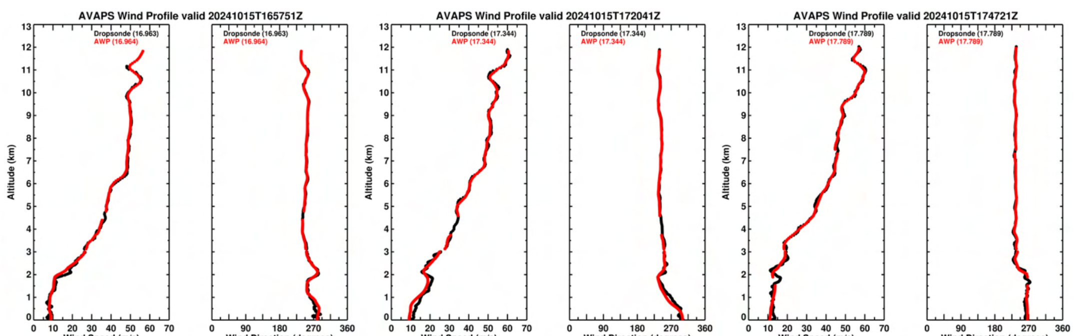

Figure 17: Co-located AWP (red) and AVAPS (black) dropsonde wind speed and direction profiles for sondes released at 1657 (left), 1720 (middle), and 1747 UTC (right).

https://doi.org/10.5194/egusphere-2026-4872
Preprint. Discussion started: 19 August 2026

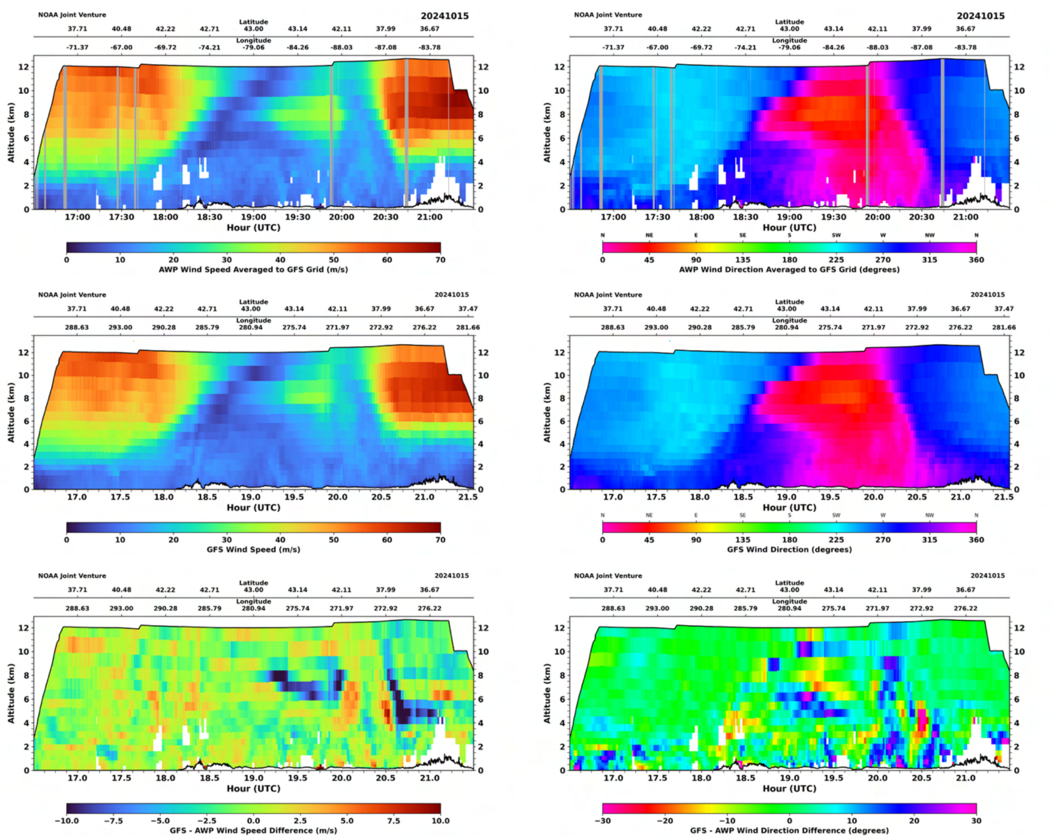

Figure 18: (top) AWP wind speed (left) and direction (right) derived from U- and V-component retrievals, averaged to the 0.25° GFS resolution along the G-3 aircraft track for the 15 October 2024 flight. (middle) GFS model wind speed and direction analysis from the 18 UTC initial analysis on 15 October along flight track. (bottom) The difference between AWP and GFS wind speed and direction.

5. Summary

5.1. AWP Instrument and Initial Flight Test Results

This is the first of a two paper series that describes the NASA airborne Aerosol Wind Profiler (AWP) Doppler wind lidar instrument, and aerosol/cloud backscatter intensity and 3-D wind profile retrieval methods applied to data collected during AWP's first science campaigns, the NOAA Joint Venture 3-D Wind Demonstration and NASA WH^{2}yMSIE/APEX that occurred in Fall 2024. AWP uses optical heterodyning with a local oscillator reference laser to detect backscattered light intensity and frequency. AWP directs laser light into two beam expanding telescopes mounted in parallel, one of which directs the light into a prism scanning mechanism that deflects the beam 30° off-nadir for vertical profiling of horizontal wind vectors, while the other beam is directed nadir which respect to the instrument orientation for profiling of vertical winds. After removal of the aircraft motion contribution to the observed Doppler shift detected per LOS, AWP measured 3-D wind vectors by combining LOS wind speed profiles from three orthogonally-oriented azimuths centered on the aircraft heading. Data processing and scanning/sampling settings used at the time of data collection enables profiling of relative aerosol backscatter (via SNR) and wind vectors with variable

https://doi.org/10.5194/egusphere-2026-4872
Preprint. Discussion started: 19 August 2026

horizontal spacing depending on selected dwell time per LOS. Dwell time was 7 secs per LOS for many flights, corresponding to ≤ 2 km spacing between profiles, while other flights featured dwells ranging from 1 to 15 secs/LOS. Winds were retrieved with 66-133 meter vertical bin spacing, with the opportunity for reduced spacing via oversampling. Wind retrievals were calibrated using land surface returns to achieve ≤ 0.1 m/s uncertainty in land speed measurements. This paper provides the first examples of AWP vertical motion retrievals to date.

AWP data from two G-3 flights are shown to demonstrate aerosol and wind profiling capabilities. Results from the 15 November 2024 cross-country transit flight illustrate the significant impact of CDWL signal integration duration on retrieval success rate. The vertical coverage of successful retrieval increased by 59% by increasing integration duration from 0.25 sec to 15 sec. Coverage increased by an additional 8% through integrating signal over a 2x deeper (133 m) atmospheric layer Another flight over the Northeast U.S. on 15 October 2024 showed complex wind, aerosol, and cloud structures associated with a jet stream and upper-tropospheric trough weather pattern. The most notable vertical motions exceeding 1 m/s were found within and above the PBL, and also within mountain waves that perturbed motions over a ~7 km deep layer extending up to flight level. AWP pulses penetrated several kilometers into stratus and cirrus clouds that featured predominantly downward motions from falling hydrometeors. There was strong agreement between AWP and AVAPS dropsonde wind profiles during the flight. GFS showed also good qualitative agreement with wind fields depicted by AWP. Comparisons with AVAPS and GFS are further presented in Part II of the paper.

Experiences with AWP add to the body of literature demonstrating the utility of CDWL technology for precise and detailed atmospheric dynamics measurements, especially within the PBL where wind observations are currently lacking or inadequate. LaRC is continuing technology and instrument development to maintain and advance airborne wind profiling capabilities over the coming decade. LaRC is currently building a copy of the AWP transceiver on an Invar optical bench which will permit up to 50% greater pulse energy to improve aerosol backscatter sensitivity and wind retrieval success rate, while reducing horizontal profile spacing because shorter integration will be required to measure sufficient backscatter signal. Increased energy coupled with a modified AWP scan strategy, where each off-nadir azimuth is sampled for ≤ 1 sec, would also offer the potential for very-high resolution (< 1 km spacing) wind retrievals in strong backscatter environments, while multiple successive scans can be integrated to improve sensitivity to weak backscatter.

5.2. A Vision for a Space-Based CDWL

Initial orbital CDWL instrument and mission design studies are underway (e.g. Marketon et al. 2024; Bedka et al. 2025). NASA ESTO and LaRC have supported development of a CDWL transceiver by Beyond Photonics, Inc. that has demonstrated 65 mJ pulse energy at 400 Hz, with 90% volume reduction, 66% mass reduction, and 3x improvement in electrical to optical system power efficiency relative to the current AWP transceiver (Diamond et al. 2024; Henderson et al. 2025). Development of wider-bandwidth receiver technology (e.g. 4 GHz) would enable measurement of molecular backscatter at 2.053 µm, leading to a calibrated AWP aerosol backscatter measurement and potentially a wind measurement from molecular backscatter (e.g. Chouza et al. 2017). We envision an orbital CDWL operating aboard a SmallSat spacecraft with two orthogonally-oriented telescopes (≥ 50 cm primary aperture)

https://doi.org/10.5194/egusphere-2026-4872
Preprint. Discussion started: 19 August 2026

to collect vector wind measurements with 10-100 km horizontal spacing and 0.1-1 km vertical spacing. These resolutions and AWP-demonstrated measurement precision meet NOAA and many Decadal Survey requirements. The ranges in spacing depend on aerosol backscatter conditions and the science requirements of the mission. A Doppler Lidar Simulation Model (SWA 2025), assuming a 400 km satellite orbit, 60 cm telescope aperture, 60 mJ pulse energy, 400 Hz rep rate, and NASA Global Modeling and Assimilation Office (GMAO) GEOS-5 Nature Run (G5NR, Castellanos et al. 2018) aerosol backscatter profiles, found that such a CDWL would achieve 30-85% wind retrieval success rate throughout the troposphere and lower stratosphere (surface to 16 km altitude) with 40 km spacing between profiles (Bedka et al. 2025). The greatest success rate was within and near to the Planetary Boundary Layer (PBL, 0-2 km altitude) and lowest success in the lower stratosphere. Above 16 km, the success rate steadily decreased up to a 20 km altitude where the modeled aerosol backscatter greatly diminished.

Data compression is required to downlink the high data volume of raw lidar signals and permit advanced CDWL wind retrievals at a variety of spatial scales. For example, NWP models may seek wind data at relatively coarse spatial scales, but with as much vertical coverage of successful wind retrieval as possible, which would necessitate longer integration and over deeper vertical layers. The PBL and weather research communities would likely desire shorter spatial scales that emphasize the PBL where aerosol concentrations are typically greatest, permitting shorter and shallower integration to achieve a successful retrieval. If downlink of all raw data is impractical, retrieval could be performed onboard the spacecraft and immediately downlinked.

We envision that the instrument could be affordably built to enable a constellation of orbital CDWLs. More frequently updating measurements would have an even greater impact on process studies, NWP, and other orbital wind profile measurements. Additional work is needed within a funded mission program to achieve a final design and mature required technologies and algorithms. An OSSE is needed to quantify the optimal number of satellites for a constellation and potential forecast impact. An orbital wind lidar could also be used to improve other space-based wind measurements. Previous studies have shown the value of lidars for characterizing AMV height assignment uncertainty (Folger and Weissmann 2016), optimizing AMV algorithms (Apke et al. 2021), reducing wind profile bias, and improving quality control of IR sounder 3-D wind profiles via machine learning (Nguyen et al 2024).

Data Availability Statement

AWP and AVAPS data from the NOAA Joint Venture 3-D Wind Demonstration and WH^{2}yMSIE/APEX are available at the NASA LaRC Suborbital Science Data for Atmospheric Composition archive: https://www-air.larc.nasa.gov/cgi-bin/ArcView/whymsie?G3=1

Author Contributions

K.B. is the science PI for AWP, and led instrument operations aboard the aircraft, and development of AWP retrievals and scientific analysis with K. K and J. C. J.M. is the engineering PI for AWP, and led engineering development by A. E. and aircraft integration with M. C. and A. N. M. C. and A. N. also provided electronics support. S. B. developed instrument control and data collection software modules. S. A. led laser integration and optimization, in collaboration with F. G. W. and A. T. F. G. W. also optimized telescope performance. S. H. led

https://doi.org/10.5194/egusphere-2026-4872
Preprint. Discussion started: 19 August 2026

development of several laser modules in with J. D. and P. K. M. K. provided team leadership and guided laser development activities during the Wind-SP program. G. D. E. and S. G. provided analyses to set AWP measurement requirements and support for scientific analysis of wind retrievals.

Acknowledgements

We thank the NASA LaRC AWP engineering team for their excellence and dedication with building and optimizing AWP for aircraft operation. We thank recently retired members of the LaRC AWP team, Michael Kavaya, Jirong Yu, Larry Petway, Teh-Hwa Wong, and Charles Boyer for their pioneering efforts with Doppler wind lidar and AWP instrument development. We thank Greg Crowther for his engineering support. We thank the LaRC Research Services Directorate and lead mission pilot Patrick Bookey for their work on successful AWP integration aboard the Gulfstream-3, and successful aircraft operations across many research flights. We thank Amin Nehrir and the HALO team for generating HALO data products used to analyze AWP data quality, and for Amin's leadership of the WH^{2}yMSIE/APEX campaign. We thank Ewan Crosbie for his extensive efforts with WH^{2}yMSIE/APEX flight planning. We thank the NASA Earth Science Division (ESD), the ESD Weather and Atmospheric Dynamics Focus Area, and ESTO for their investments to support the Wind-SP and AWP programs. We also acknowledge the NASA Joint Venture Program for supporting the AWP 3-D Wind Demonstration project.

Financial support

Wind-SP and AWP instrument development was supported by directed funding from the NASA Earth Science Technology Office and Earth Science Division. AWP flight operations and data analysis was supported by agreement number OSAAPIAA 2016-000 0002 with the NOAA Systems Architecture and Engineering Office, NESDIS Joint Venture Partnerships.

List of Acronyms and Abbreviations

AA – Automatic-Alignment	INS – Inertial Navigation System
ALADIN - Atmospheric LAser Doppler Instrument	LaRC – Langley Research Center (NASA)
AMV – Atmospheric Motion Vector	LC – Left Circular Polarization
AOM – Acousto-optic Modulator	LCM – Laser Control Module
APEX – Active Passive PBL Profiling Experiment	LEM – Local Electronics Module
AVAPS - Airborne Vertical Atmospheric Profiling System	LO – Local Oscillator (CW laser)
AWP – Aerosol Wind Profiler (LaRC)	LOS – Line-Of-Sight
BPLO – Back-Propagating Local Oscillator	LPM – Low-Power Module
CaF – Calcium-Flouride	MO – Master Oscillator (CW laser, seed laser)
Cal/Val – Calibration and Validation	MOPA – Master Oscillator Power Amplifier

https://doi.org/10.5194/egusphere-2026-4872
Preprint. Discussion started: 19 August 2026

CDWL – Coherent Doppler Wind Lidar	NASA – National Aeronautics & Space Administration
CFC – Carbon Fiber Composite	NED – North-East-Down Coordinate System
CNR – Carrier-to-Noise Ratio	NESDIS - National Environmental Satellite, Data, and Information Service (NOAA)
CW – Continuous Wave	NOAA – National Oceanic and Atmospheric Administration
DAWN – Doppler Aerosol WiNd (lidar) (LaRC)	NSOSA - NOAA Satellite Observing System Architecture study
DIAL – Differential Absorption Lidar	NWP – Numerical Weather Prediction
DLR - Deutsches Zentrum für Luft- und Raumfahrt (German Aerospace Center)	OAWL – Optical Auto-covariance Wind Lidar
DWL – Doppler Wind Lidar	OSE – Observing System Experiment
ECMWF – European Center for Medium Range Weather Forecasting	OSSE – Observing System Simulation Experiment
ESA – European Space Agency	PAN - Polyacrylonitrile
ESD – Earth Science Division (NASA SMD)	PBL – Planetary Boundary Layer
ESTO – Earth Science Technology Office (NASA ESD)	PBS – Polarizing Beam Splitter
ETOPO – Earth TOPOgraphy	PRF – Pulse Repetition Frequency
FFT – Fast Fourier Transform	RC – Right Circular Polarization
G-3 – Gulfstream-3 (NASA LaRC)	RMS – Root (of the) Mean (of the) Squares
GFS – Global Forecast System	RMSD – Root (of the) Mean (of the) Squares Difference
GMAO – Global Modeling and Assimilation Office (NASA)	Rx - Receive
GOES – Geostationary Operational Environmental Satellite	SMD – Science Mission Directorate (NASA)
GPS – Global Positioning System	SNR – Signal-to-Noise Ratio
GRIP – Genesis and Rapid Intensification Process (NASA)	SP – Space Pathfinder
GSFC – Goddard Space Flight Center	SWIFT – Super-Wide Frequency-Tunable laser (Beyond Photonics)
GWOS – Global Wind Observing System	TFOM – Transmitter Figure of Merit
HALO – High Altitude Lidar Observatory	TRL – Technology Readiness Level
HPM – High-Power Module	Tx - Transmit
HR – Highly Reflective	3-D – Three Dimensional
HRRR – High Resolution Rapid Refresh model (NOAA)	UTC – Universal Time Coordinate

https://doi.org/10.5194/egusphere-2026-4872
Preprint. Discussion started: 19 August 2026

HSRL – High Spectral Resolution Lidar	WDM – Wavelength Division Multiplexer
IF – Intermediate Frequency	WH^{2}YMSIE - Westcoast & Heartland Hyperspectral Microwave Sensor Intensive Experiment (NASA)
InGaAs - Indium Gallium Arsenide	

References

Apke, J. M., Noh, Y., and Bedka, K.: Comparison of Optical Flow Derivation Techniques for Retrieving Tropospheric Winds from Satellite Image Sequences. *J. Atmos. Oceanic Technol.*, **39**, 2005–2021, https://doi.org/10.1175/JTECH-D-22-0057.1., 2022

Atlas, R., and Coauthors: Observing system simulation experiments (OSSEs) to evaluate the potential impact of an Optical Autocovariance Wind Lidar (OAWL) on numerical weather prediction. *J. Atmos. Oceanic Technol.*, ***32***, 1593-1613, https://doi.org/10.1175/JTECH-D-15-0038.1., 2015

Baker, W. E., and Coauthors: Lidar-measured wind profiles: The missing link in the global observing system. *Bull. Amer. Meteor. Soc.*, ***95***, 543–564, https://doi.org/10.1175/BAMS-D-12-00164.1., 2014

Baron, P., Ishii. S., Okamoto, K., Gamo, K., Mizutani, K., Takahashi, C., Itabe, T., Iwasaki, T., Kubota, T., Maki, T., Oki, R., Ochiai, S., Sakaizawa, D., Satoh, M., Satoh, Y., Tanaka, T. Y., and Yasui, M.: Feasibility study for future spaceborne coherent Doppler wind lidar. Part 2: Measurement simulation algorithms and retrieval error characterization. *J. Meteor. Soc. Japan*, **95**, 319-342. https://doi.org/10.2151/jmsj.2017-018, 2017

Bedka, K. M., Nehrir, A. R., Kavaya, M., Barton-Grimley, R., Beaubien, M., Carroll, B., Collins, J., Cooney, J., Emmitt, G. D., Greco, S., Kooi, S., Lee, T., Liu, Z., Rodier, S., and Skofronick-Jackson, G.: "Airborne lidar observations of wind, water vapor, and aerosol profiles during the NASA Aeolus calibration and validation (Cal/Val) test flight campaign," Atmos. Meas. Tech., 14 (6), 4305–4334, (2021) https://doi.org/10.5194/amt-14-4305-2021, 2021

Bedka, K. M, Marketon, J., Henderson, S., Kavaya, M.: AWP: NASA's Aerosol Wind Profiler Coherent Doppler Wind Lidar. In: Singh, U.N., Tzeremes, G., Refaat, T.F., Ribes Pleguezuelo, P. (eds) Space-based Lidar Remote Sensing Techniques and Emerging Technologies. LIDAR 2023. Springer Aerospace Technology. Springer, Cham. https://doi.org/10.1007/978-3-031-53618-2_3, 2024

Bedka, K. M. and Co-Authors: 3-D Lidar Wind Airborne Profiling Using A Coherent-Detection Doppler Wind Lidar Designed For Space-Based Operation: Final Project Report in Response to: "Measuring the Atmospheric Wind Profile (3D Winds): Call for Studies and Field Measurement Campaigns". Available online at: https://doi.org/10.25923/6njy-ke16, 2025

Castellanos, P., Da Silva, A.M., Darmenov, A.S., Buchard, V., Govindaraju, R.C., Ciren, P. and Kondragunta, S.: A geostationary instrument simulator for aerosol observing system simulation experiments. *Atmosphere*, 10(1), https://www.mdpi.com/2073-4433/10/1/2, 2018

Chouza, F., Witschas, B. B., and Reitebuch, O.: Heterodyne high spectral resolution lidar, *Appl. Opt.*, 56, 8121 – 8134, 2017

Coniglio, M. C., and Parker, M. D.: Insights into Supercells and Their Environments from Three Decades of Targeted

https://doi.org/10.5194/egusphere-2026-4872
Preprint. Discussion started: 19 August 2026

Radiosonde Observations. *Mon. Wea. Rev.*, **148**, 4893–4915, https://doi.org/10.1175/MWR-D-20-0105.1. 2020

DeLange, O., 1968: Optical heterodyne detection. *IEEE Spectrum*, *5*, 77–85. https://ieeexplore.ieee.org/stamp/stamp.jsp?tp=&arnumber=5215385

Diamond, J., Fernandez, P. A., and Henderson, S.: Compact High-Power 2-micron Transmitter for Coherent Lidar Applications. 2024 Coherent Laser Radar Conference, Landshut, Germany (June 23-28, 2024). https://beyondphotonics.com/wp-content/themes/beyondphotonics/img/CLRC_2024-Compact_Transmitter.pdf, 2024

Dolfi-Bouteyre, A., and Co-Authors: Pulsed 1.5-um LIDAR for axial aircraft wake vortex detection based on high-brightness large-core fiber amplifier, *IEEE Journal of Selected Topics in Quantum Electronics* 15, 441–450, 2009

DuVivier, A. K., Cassano, J. J., Greco, S., and Emmitt, G. D.: A Case Study of Observed and Modeled Barrier Flow in the Denmark Strait in May 2015. *Mon. Wea. Rev.*, 145, 2385–2404, https://doi.org/10.1175/MWR-D-16-0386.1. 2017

Engin, D., Rudd, W., Storm, M., Long, M., Litvinovitch, V., Holley, L., and Sawruk, N. W.: High Power Thulium Fiber Laser Systems for Airborne and Spaceborne Missions," *Proc. SPIE 11261, Components and Packaging for Laser Systems VI* (2020); https://doi.org/10.1117/12.2547955 2020

ESA, 2023: https://www.esa.int/Applications/Observing_the_Earth/FutureEO/Aeolus/Trailblazing_Aeolus_mission_winding_down#:~:text=On%2030%20April%202023%2C%20all,end%2Dof%2Dlife%20activities

Eyre, J.R., Bell, W., Cotton, J., English, S.J., Forsythe, M., Healy, S.B., and Co-authors: Assimilation of satellite data in numerical weather prediction. Part II: Recent years. *Q J R Meteorol Soc*, 521–556. Available from: https://doi.org/10.1002/qj.4228, 2022

Feltz, W. F., Bedka, K. M., Otkin, J. A., Greenwald, T., and Ackerman, S. A.: Understanding Satellite-Observed Mountain-Wave Signatures Using High-Resolution Numerical Model Data. *Wea. Forecasting*, **24**, 76–86, https://doi.org/10.1175/2008WAF2222127.1, 2009

Feng, C. Pu, Z., Nehrir, A. R., Bedka, K. M., and Doyle, J.: Benefits of Assimilating DAWN and HALO Observations on Numerical Simulations of Tropical Convective Systems Associated with African Easterly Waves During NASA's CPEX-AW and CPEX-CV. *J. Atmos. Oceanic Technol.*, **42**, 1419–1444, https://doi.org/10.1175/JTECH-D-24-0138.1, 2025

Flament, T., Trapon, D., Lacour, A., Dabas, A., Ehlers, F., and Huber, D.: Aeolus L2A aerosol optical properties product: standard correct algorithm and Mie correct algorithm, Atmos. Meas. Tech., 14, 7851–7871, https://doi.org/10.5194/amt-14-7851-2021, 2021

Folger, K. and Weissmann, M.: Height correction of atmospheric motion vectors using satellite lidar observations from CALIPSO. *Journal of Applied Meteorology and Climatology*, **53**, 1809–1819. https://doi.org/10.1175/JAMC-D-13-0337.1, 2014

Frehlich, R., Hannon, S. M., and Henderson, S. W.: Performance of a 2-µm Coherent Doppler Lidar for Wind Measurements. *J. Atmos. Oceanic Technol.*, **11**, 1517–1528, https://doi.org/10.1175/1520-0426(1994)011<1517:POACDL>2.0.CO;2, 1994

https://doi.org/10.5194/egusphere-2026-4872
Preprint. Discussion started: 19 August 2026

Frehlich, R., Hannon, S. M., and Henderson, S. W.: Coherent Doppler lidar measurements of winds in the weak signal regime, *Appl. Opt.*, 36, 3491-3499, 1997

Frehlich, R., 2004: Velocity Error for Coherent Doppler Lidar with Pulse Accumulation. *J. Atmos. Oceanic Technol.*, **21**, 905–920, https://doi.org/10.1175/JTECH1596.

Greco, S., Emmitt, G.D., DuVivier, A., Hines, K., Kavaya, M.: Polar Winds: Airborne Doppler Wind Lidar Missions in the Arctic for Atmospheric Observations and Numerical Model Comparisons. *Atmosphere*, 11, 1141. https://doi.org/10.3390/atmos11111141, 2020a

Greco, S.; Emmitt, G. D., Garstang, M., and Kavaya, M.: Doppler Aerosol WiNd (DAWN) Lidar during CPEX 2017: Instrument Performance and Data Utility. *Remote Sens.* 2020, 12, 2951. https://doi.org/10.3390/rs12182951, 2020b

Heliere, A., Wernham, D., Mason, G., De Villele, G., and Co-Authors: Status of Aeolus-2 mission pre-development activities, *Proc. SPIE 12777, International Conference on Space Optics — ICSO 2022*, 1277709, https://doi.org/10.1117/12.2688794, 2023

Henderson, S.W., Yuen, E., and Fry, E. S.: Fast resonance-detection technique for single-frequency operation of injection-seeded Nd:YAG lasers, *Opt. Lett.*, 11, 715 – 717, 1986

Henderson, S., Gatt, P., Rees, D., and Huffaker, R. M.: Wind Lidar. Book Chapter 7 in *Laser Remote Sensing (1st ed.)*. CRC Press. Fujii, T., & Fukuchi, T. (Editors). https://doi.org/10.1201/9781420030754, 2005

Henderson, S. W. and Hale, C. P.: Fast widely-tunable single-frequency 2-micron laser for remote-sensing applications, *Proc. SPIE 10406, Lidar Remote Sensing for Environmental Monitoring 2017*, 104060C (30 August 2017); https://doi.org/10.1117/12.2277089, 2017

Henderson, S.W., Kratovil, P. T., and Hale, C. P.: Antenna Efficiency Optimization in Coherent Lidar Systems, *19th Coherent Laser Radar Conference*, Okinawa Japan, 18-21 June 2018. Paper available at: http://beyondphotonics.com/publications/, 2018a

Henderson, S.W., Jacob, D.: Space-Based Coherent Lidar for Wind Measurements with High-Percentage Tropospheric Coverage, *19th Coherent Laser Radar Conference*, Okinawa Japan, 18-21 June 2018. Paper available at http://beyondphotonics.com/publications/, 2018b

Henderson, S. W., Kavaya, M., Yu, J., Kratovil, P., Hale, C., and Co-Authors: Advanced Eyesafe Lidar for Atmospheric Wind Measurements. 2022 Coherent Laser Radar Conference, Big Sky, Montana (June 26 – July 1, 2022). https://beyondphotonics.com/wp-content/themes/beyondphotonics/img/CLRC_2022-Wind-SP_Tech.pdf, 2022

Henderson, S. W., Diamond, J., Alvarez, P., and Kratovil, P.: Technology Advances for Airborne and Space-Based Coherent Lidar for Atmospheric Wind Measurements. 2025 NOAA-NASA Space-Based Wind Workshop. College Park, Maryland. (February 19-20 2025) https://beyondphotonics.com/wp-content/themes/beyondphotonics/img/3D_Winds_2025-Coherent_Lidar_Tech_Advances.pdf, 2025

Hristova-Veleva, S., Zhang, S. Q., Turk, F. J., Haddad, Z. S., and Sawaya, R. C.: Assimilation of DAWN Doppler wind lidar data during the 2017 Convective Processes Experiment (CPEX): impact on precipitation and flow structure, *Atmos. Meas. Tech.,* 14, 3333–3350, https://doi.org/10.5194/amt-14-3333-2021, 2021

https://doi.org/10.5194/egusphere-2026-4872
Preprint. Discussion started: 19 August 2026

Ishii, S., Baron, P., Aoki, M., Mizutani, K., Yasui, M., Ochiai, S., and Co-Authors: Feasibility study for future space-borne coherent Doppler wind lidar, Part 1: Instrumental overview for global wind profile observation. *J. Meteor. Soc. Japan*, **95**, 301-317. https://doi.org/10.2151/jmsj.2017-017, 2017

Karpowicz, B. M., and Privé, N. C.: Using the GEOS-5 Nature Run to Simulate 2053-nm Coherent Doppler Wind Lidar Observations. *J. Atmos. Oceanic Technol.*, **41**, 665–683, https://doi.org/10.1175/JTECH-D-23-0117.1, 2024

Kavaya, M. J., Beyon, J. Y., Koch, G. J., Petros, M., Petzar, P., Singh, U. N., Trieu, B. C., and Yu, J.: The Doppler Aerosol Wind (DAWN) Airborne, Wind-Profiling Coherent-Detection Lidar System: Overview and Preliminary Flight Results. *J. Atmos. Oceanic Technol.*, **31**, 826–842, https://doi.org/10.1175/JTECH-D-12-00274.1, 2014

Lux, O., Lemmerz, C., Weiler, F., Marksteiner, U., Witschas, B., Rahm, S., Geiß, A., Schäfler, A., and Reitebuch, O.: Retrieval improvements for the ALADIN Airborne Demonstrator in support of the Aeolus wind product validation, *Atmos. Meas. Tech.*, 15, 1303–1331, https://doi.org/10.5194/amt-15-1303-2022, 2022

Lux, O., Rennie, M., de Kloe, J., and Reitebuch, O.: Five years of Aeolus wind profiling: global coverage and data quality, *Atmos. Meas. Tech.*, 19, 1729–1761, https://doi.org/10.5194/amt-19-1729-2026, 2026

Ma, Z., Riishøjgaard, L. P, Masutani, M., Woollen, J. S., and Emmitt, G. D.: Impact of Different Satellite Wind Lidar Telescope Configurations on NCEP GFS Forecast Skill in Observing System Simulation Experiments. *J. Atmos. Oceanic Technol.*, **32**, 478–495, https://doi.org/10.1175/JTECH-D-14-00057.1, 2015

Marketon, J. E., Bedka, K. M., Henderson, S., Khlopenkov, K., Cooney, J.: Coherent Doppler Wind Lidar Suborbital and Orbital Activities at NASA Langley Research Center. *2024 Coherent Laser Radar Conference*, Landshut, Germany (June 23-28, 2024). Available online: https://ntrs.nasa.gov/citations/20240007658, 2024

Marseille, G. J., Stoffelen, A., and Barkmeijer, J.: A cycled sensi-tivity observing system experiment on simulated Doppler wind li-dar data during the 1999 Christmas storm “Martin” . *Tellus 60A*, DOI: https://doi.org/10.1111/j.1600-0870.2007.00290.x, 2007

Marseille, G. J., Stoffelen, A., and Barkmeijer, J.: Impact assessment of prospective spaceborne Doppler wind lidar observation scenarios. *Tellus A: Dynamic Meteorology and Oceanography*, *60*(2), 234–248. https://doi.org/10.1111/j.1600-0870.2007.00289.x, 2008

Mazza, E., and Chen, S. S.: Compound dry-dusty air intrusions during the genesis of Tropical Storm Kate (2021): Observations from the CPEX-AW field campaign and coupled modeling. *Journal of Geophysical Research: Atmospheres*, 130, e2024JD042653. https://doi.org/10.1029/2024JD042653, 2025

McCarty, W., Carvalho, D., Moradi, I., and Privé, N. C.: Observing system simulation experiments investigating atmospheric motion vectors and radiances from a constellation of 4–5-μm infrared sounders. *J. Atmos. Oceanic Technol.*, ***38***, 331–347, https://doi.org/10.1175/JTECH-D-20-0109.1, 2021

National Academies of Sciences, Engineering, and Medicine (NASEM): *Thriving on Our Changing Planet: A Decadal Strategy for Earth Observation from Space*. Washington, DC: The National Academies Press. https://doi.org/10.17226/24938, 2018

Nguyen, H., Posselt, D., Yanovsky, I., Wu, L., and Hristova-Veleva, S.: Atmospheric motion vector (AMV) error characterization and bias correction by leveraging independent lidar data: a simulation using an observing system

https://doi.org/10.5194/egusphere-2026-4872
Preprint. Discussion started: 19 August 2026

simulation experiment (OSSE) and optical flow AMVs, *Atmos. Meas. Tech.*, 17, 3103–3119, https://doi.org/10.5194/amt-17-3103-2024, 2024

Nixon, C. J., and Allen, J. T.: Distinguishing between Hodographs of Severe Hail and Tornadoes. *Wea. Forecasting*, **37**, 1761–1782, https://doi.org/10.1175/WAF-D-21-0136.1, 2022

NOAA NCEI: ETOPO 2022 15 Arc-Second Global Relief Model. NOAA National Centers for Environmental Information. DOI: 10.25921/fd45-gt74, 2022

NOAA NESDIS: The NOAA Satellite Observing System Architecture (NSOSA) Study, NOAA-NESDIS-2018-0053-0002 (May 31, 2018); https://www.regulations.gov/document/NOAA-NESDIS-2018-0053-0002, 2018

NOAA NESDIS: Broad Agency Announcement: Measuring the Atmospheric Wind profile (3D Winds): Call for Studies and Field Measurement Campaigns for NOAA/NESDIS; https://sam.gov/opp/058f74a44553411d9f50417a315e745f/view, 2022

Nowottnick, E. P., and Co-Authors: Dust, Convection, Winds, and Waves: The 2022 NASA CPEX-CV Campaign. *Bull. Amer. Meteor. Soc.*, 105, E2097–E2125, https://doi.org/10.1175/BAMS-D-23-0201.1, 2024

NSF NCAR - Earth Observing Laboratory: NCAR Airborne Vertical Atmospheric Profiling System (AVAPS). NSF NCAR - Earth Observing Laboratory. https://doi.org/10.5065/D66W9848, 1993

Okamoto, K., Ishibashi, T., Ishii, S., Baron, P., Gamo, K., Tanaka, T. Y., Yamashita, K., and Kubota, T.: Feasibility Study for Future Space-Borne Coherent Doppler Wind Lidar, Part 3: Impact Assessment Using Sensitivity Observing System Simulation Experiments, *J. Meteorol. Soc. Jpn.*, 96, 179–199, https://doi.org/10.2151/jmsj.2018-024, 2018

Ouyed, A., Zeng, X., Wu, W., Lei, L., Liu, X., and Xu, Y.: 0.25 deg horizontal winds and derived dynamic quantities from NOAA-20 and Suomi-NPP satellite water vapor soundings. *Geophysical Research Letters*, 52, e2025GL119334. https://doi.org/10.1029/2025GL119334, 2025

Pagano, T. J., Waliser, D. E., Guan, B., Ye, H., Ralph, F. M., and Kim, J: Extreme Surface Winds during Landfalling Atmospheric Rivers: The Modulating Role of Near-Surface Stability. *J. Hydrometeor.*, **22**, 1681–1693, https://doi.org/10.1175/JHM-D-20-0165.1, 2021

Rennie, M. P., Isaksen, L., Weiler, F., de Kloe, J., Kanitz, T., and Reitebuch, O.: The impact of Aeolus wind rerievals on ECMWF global weather forecasts. *Quart. J. Roy. Meteor. Soc.*, ***147***, 3555–3586, https://doi.org/10.1002/qj.4142., 2021

Rennie, M.: A consolidated assessment of the impact of Aeolus winds in NWP at ECMWF. *2023 Aeolus Science Conference*. Rhodes, Greece, 24 May 2023. Available online at: https://www.dropbox.com/s/ps1y18kpvv219cj/1.%20ECMWF_NWP_impact_Aeol_winds_Rennie_Rhodes_sci_conf.pdf?dl=0, 2023

Rew, R. L., Johnson, B., Gibson, B., and Mohamed, A.: A review of airborne Doppler lidar for wind-sensing. *Progress in Aerospace Sciences*, 157, https://doi.org/10.1016/j.paerosci.2025.101127, 2025

Riishojgaard, L. P., Ma, Z., Masutani, M., Woollen, J. S., Emmitt, G. D., Wood, S. A., and Greco, S.: Observation system simulation experiments for a global wind observing sounder. *Geophys. Res. Lett.*, ***39***, L17805, doi:10.1029/2012GL051814, 2012

https://doi.org/10.5194/egusphere-2026-4872
Preprint. Discussion started: 19 August 2026

Rios-Berrios, R., Finocchio, P. M., Alland, J. J., Chen, X., Fischer, M. S., Stevenson, S. N., and Tao, D.: A Review of the Interactions between Tropical Cyclones and Environmental Vertical Wind Shear. *J. Atmos. Sci.*, **81**, 713–741, https://doi.org/10.1175/JAS-D-23-0022.1, 2024

Rye, B.J, 1982: Primary aberration contribution to incoherent backscatter heterodyne returns, *Appl. Opt.* 21, 839-844

Sakaeda, N., and Co-Authors: Synoptic Influences on the Diurnal Cycle of Rainfall over Western Puerto Rico. *Mon. Wea. Rev.*, **152**, 2341–2359, https://doi.org/10.1175/MWR-D-24-0035.1, 2024

Sakaeda, N., and Co-Authors: Synoptic Modulation of the West African Coastal Atmosphere and Mesoscale Convective Systems. *Mon. Wea. Rev.*, **153**, 1939–1957, https://doi.org/10.1175/MWR-D-24-0281.1, 2025

Santek, D., Nebuda, S., and Stettner, D.: Demonstration and evaluation of 3D winds generated by tracking features in moisture and ozone fields derived from AIRS sounding retrievals. *Remote Sens.*, ***11***, 2597, https://doi.org/10.3390/rs11222597, 2019

Singh, U. N., Walsh, B. M., Yu, J., Petros, M., Kavaya, M. J., Refaat, T. F., and Barnes, N. P.: Twenty years of Tm:Ho:YLF and LuLiF laser development for global wind and carbon dioxide active remote sensing, *Opt. Mater. Express,* 5, 827-837, 2015

Stoffelen, A., and Co-Authors: Wind Profile Satellite Observation Requirements and Capabilities. *Bull. Amer. Meteor. Soc.*, **101**, E2005–E2021, https://doi.org/10.1175/BAMS-D-18-0202.1, 2020

Straume-Lindner, A.G., and Co-Authors: ESA'S Wind Mission Aeolus - Overview, Status and Outlook, *2021 IEEE International Geoscience and Remote Sensing Symposium IGARSS*, Brussels, Belgium, 2021, pp. 755-758, doi: 10.1109/IGARSS47720.2021.9554007. https://ieeexplore.ieee.org/document/9554007, 2021

SWA: https://swa.com/images/LidarSpaceBased/TheDopplerLidarSimulationModel.pdf, 2025

Taszarek, M., and Co-Authors: What do large hail, tornado, and severe thunderstorm wind environments have in common across continents?. *Bull. Amer. Meteor. Soc.*, BAMS-D-25-0268.1, https://doi.org/10.1175/BAMS-D-25-0268.1, in press, 2026.

Teixeira, J., and Co-Authors: Toward a Global Planetary Boundary Layer Observing System: A Summary. *Bull. Amer. Meteor. Soc.*, **106**, E1566–E1579, https://doi.org/10.1175/BAMS-D-23-0228.1, 2025

Turk, F. J., Hristova-Veleva, S., Durden, S. L., Tanelli, S., Sy, O., Emmitt, G. D., Greco, S., and Zhang, S. Q.: Joint analysis of convective structure from the APR-2 precipitation radar and the DAWN Doppler wind lidar during the 2017 Convective Processes Experiment (CPEX), *Atmos. Meas. Tech.*, 13, 4521–4537, https://doi.org/10.5194/amt-13-4521-2020, 2020

Uhlenbrock, N. L., Bedka, K. M., Feltz, W. F., and Ackerman, S. A.: Mountain Wave Signatures in MODIS 6.7-µm Imagery and Their Relation to Pilot Reports of Turbulence. *Wea. Forecasting*, **22**, 662–670, https://doi.org/10.1175/WAF1007.1, 2007

Wang, J.W., 1988: Optimal truncation of a lidar transmitted beam. *Appl. Opt.*, 27, 4470–4474, 1988.

Witschas, B., Lemmerz, C., Geiß, A., Lux, O., Marksteiner, U., Rahm, S., Reitebuch, O., Schäfler, A., and Weiler, F., 2022: Validation of the Aeolus L2B wind product with airborne wind lidar measurements in the polar North Atlantic region and in the tropics, *Atmos. Meas. Tech.,* 15, 7049–7070, https://doi.org/10.5194/amt-15-7049-2022

WMO OSCAR, 2025: https://space.oscar.wmo.int/requirements

https://doi.org/10.5194/egusphere-2026-4872
Preprint. Discussion started: 19 August 2026

Yanovsky, I., Posselt, D. J., Wu, L., and Hristova-Veleva, S.: Quantifying Uncertainty in Atmospheric Winds Retrieved from Optical Flow: Dependence on Weather Regime. *J. Appl. Meteor. Climatol.*, **63**, 1113–1135, https://doi.org/10.1175/JAMC-D-23-0169.1, 2024

Yu, J., Lee, J., Wong, T.-H., Petway, L., Traore, A., Chen, S., Marketon, J., and Co-Authors: Efficient Ho:LuLiF MOPA laser transmitter for space pathfinder coherent wind lidar," Invited Paper, *2022 Coherent Laser Lidar Conference*, Big Sky, MT (June 26 – July 1, 2022) Available online at: https://ntrs.nasa.gov/api/citations/20220008811/downloads/Yu%20CLRC-2022-summary.pdf, 2022.

Zeng, X., and Co-Authors: Vientos—A New Satellite Mission Concept for 3D Wind Measurements by Combining Passive Water Vapor Sounders with Doppler Wind Lidar. *Bull. Amer. Meteor. Soc.*, 105, E357–E369, https://doi.org/10.1175/BAMS-D-22-0283.1, 2024